CHALMERS
UNIVERSITY OF TECHNOLOGY

KU LEUVEN

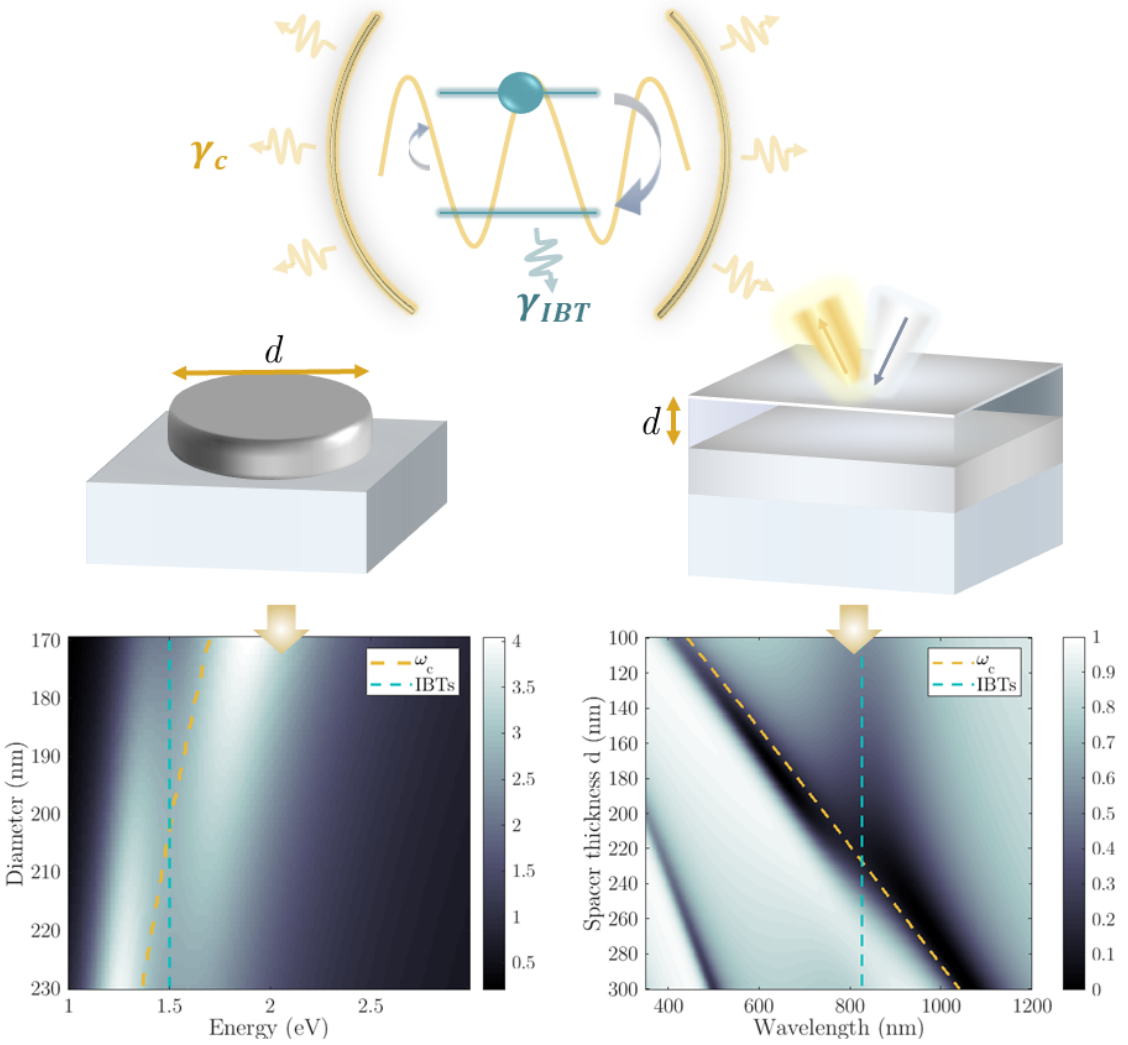

Light-Interband transitions coupling in Aluminum

Erasmus Mundus Master of Science in Nanoscience and Nanotechnology

ADRIANA IVONNE CANALES RAMOS

Department of Physics
CHALMERS UNIVERSITY OF TECHNOLOGY
Gothenburg, Sweden 2018

Co-funded by the
Erasmus+ Programme
of the European Union

Master's thesis
Erasmus Mundus Master of Science in Nanoscience and Nanotechnology

Light - Interband transitions coupling in Aluminum

ADRIANA IVONNE CANALES RAMOS

Department of Physics
Division of Bionanophotonics
Chalmers University of Technology
Gothenburg, Sweden 2018

Light-Interband transitions coupling in Aluminum

ADRIANA IVONNE CANALES RAMOS

Supervisor: Timur Shegai, Chalmers University of Technology.
Co-Promoter at KU Leuven: Bart Sorée, imec.
External examiner: Thilo Bauch, Chalmers University of Technology.

Master's Thesis 2018:NN
Division of Bionanophotonics
Department of Physics
Chalmers University of Technology
SE-412 96 Gothenburg
Telephone +46 31 772 1000

Cover: Schema of light-interband transitions (IBTs) interactions and the two cavities used to couple them: Al nanodisks (left) and asymmetric microcavities in a perfect absorber configuration (right). Calculations of the light-IBTs anticrossing in extinction (left) and reflectivity (right) for each cavity. The detuning is controlled by the diameter of the nanodisk and the thickness of the dielectric between the two mirrors, respectively.

Chalmers Reproservice
Gothenburg, Sweden 2018

Light-Interband transitions coupling in Aluminum

Adriana Ivonne Canales Ramos
Division of Bionanophotonics
Department of Physics
Chalmers University of Technology

Abstract

Light-matter interactions may be described as the energy transfer between an electronic transition (emitter or two-level system) and an optical cavity. In weak interactions such transfer is mainly from one component to the other. Thus, the transition rate of the two-level system can be changed, via the so-called Purcell effect. Whereas strong interactions are characterized by a reversible energy transfer between the components and giving rise to a hybrid system with properties different than the original components. This allows to tailor fundamental properties of matter by strongly coupling the transition to light [1].

This work studied the interaction between interband transitions (IBTs) in Aluminum and resonances of two different kind of cavities: plasmonic nanodisks and asymmetric microcavities in a perfect absorber configuration. The system is peculiar because the cavity is coupled to an intrinsic transition of the material that composes it. Calculations using Drude-Lorentz model for the dielectric function of Al were perfomed to model the coupling on both cavities. Extinction and scattering spectra were calculated for nanodisks, and reflectivity spectra for microcavities. Both systems were fabricated and optically characterized by taking extinction, scattering, and reflection spectra of the samples.

The resulting interactions between IBTs and the two cavity modes were weak, which is enough to modify the absorption rate of the IBTs, but not enough to change fundamental properties of Al. Calculations suggest that by improving Al quality during deposition, the interaction gets stronger, such that it is on the edge of strong coupling. A surprising result of this work is the potential of asymmetric microcavities as open cavities to study light-matter interactions even without the contribution of IBTs.

Keywords: Interband transitions, Aluminum nanodisks, Localized Surface Plasmon Resonance, asymmetric microcavities, perfect absorber, weak coupling, strong coupling.

Acknowledgements

I am very grateful to all the people who made this work possible. Foremost, I would like to express my gratitude to my supervisor Timur Shegai. For introducing me to the strong-coupling field, for sharing his knowledge and enthusiasm for science, for always having his door open for discussions whenever any question or new results came up, and for inviting me to all the workshops and seminars, they were an incredible source of knowledge.

I would like to thank my daily supervisor Ankit Bisht. For his infinite patience while teaching me most of the fabrication and characterization techniques used in this work. I learned from the best. In particular, thanks for the EBL nanodisks fabrication, for the inputs on this manuscript and for the amazing introduction to the cleanroom, I realized I enjoy working there. Also, for all the long discussions and for letting me be part of his research project while I learned enough to start my own, and for his guidance and help during my project. The long hours at the cleanroom and lab were more fun and interesting with our discussions about science and life.

I am grateful to Martin Wersäll for all the discussions that lead me to a better understanding of strongly coupled systems, and for his comments on this manuscript. For always listening and giving me valuable advice, for encouraging me and for helping me realize how much I enjoy science.

Thanks to Battulga Munkhbat, for showing me how to characterize nanodisks. Especially for his dedication while helping me figure out the issue with single particle measurements. For his inspiring diligence and for his word of advice.

As well as, to Ruggero Verre, for showing me the HCL fabrication process and for his ideas to make fabrication simpler. To Nils Odebo and Denis Baranov for the inputs on TMM.

Likewise, to Michael Strürenberg, Benjamin Rousseaux and, Jorge Cuadra for always being open to interesting discussions and creating a strongly-coupled group. I also appreciate the great work environment created by everyone at the Divison of Bionanophotonics.

I am also very grateful to the EMM Nano board for giving me the opportunity to come to Leuven and Chalmers with a full scholarship. Thanks to Bart Sorée for taking the role as my co-promotor in Leuven. As well as, to Thilo Bauch for all his help regarding thesis topics and for acting as external examiner of this work.

Thanks to Allan for all the comments on this thesis and for sharing this journey with me at a distance. Finally, I am deeply grateful to my parents, who have always supported my decisions, encouraging me to grow and learn.

Adriana Canales, Gothenburg, August 2018

Contents

List of Figures **xi**

1 Introduction **1**
1.1 Thesis outline . . . 2

2 On light and matter **3**
2.1 Optical Properties of Metals . . . 3
2.1.1 Drude-Lorentz model . . . 3
2.1.2 Interband Transitions of Al . . . 5
2.2 Optical Cavity Modes . . . 6
2.2.1 Plasmonic nanoresonators . . . 6
2.2.1.1 Scattering by a small oblate ellipsoid . . . 6
2.2.1.2 Modified long wavelength approximation . . . 7
2.2.2 Asymmetric microcavities . . . 8

3 Light-Matter coupling **9**
3.1 Basics on weak and strong coupling . . . 9
3.1.1 The advantage of lossy cavities . . . 11
3.2 Classical Coupled Oscillator Model . . . 11
3.3 Previously on IBT-light coupling . . . 12

4 Methods **15**
4.1 Calculations . . . 15
4.1.1 Extinction spectra of Al nanodisks . . . 15
4.1.2 Transfer Matrix Method . . . 16
4.2 Sample Fabrication . . . 17
4.2.1 Nanodisks fabrication . . . 18
4.2.1.1 Electron beam Lithography . . . 18
4.2.1.2 Hole-Mask Colloidal Lithography . . . 19
4.2.2 Asymmetric microcavities . . . 20
4.3 Optical Characterization . . . 21
4.3.1 Ensemble measurements: UV-Vis spectrophotometry . . . 22
4.3.2 Single particle measurements: Dark-Field microscopy . . . 22
4.3.3 Reflection measurements of microcavities . . . 23
4.3.4 Dispersion measurements . . . 24

5 Results **25**

5.1 LSPR coupled to interband transitions 25
5.1.1 Extinction calculations 25
5.1.2 Ensemble experiments 29
5.1.3 Single particle experiments 31
5.2 Asymmetric microcavities 33
5.2.1 Measurements of the microcavities 35
5.2.2 Molecule on top of the cavity 36
5.2.3 WSe_2 on top of the cavity 38
5.3 Potential of Light-IBT strongly coupled systems 41

6 Conclusion and Outlook **43**

References **45**

List of Figures

2.1 Al dielectric function. (a) Experimental data by Rakic [2] and Drude-Lorentz model fit, with $\hbar\omega_P = 13.3$ eV, $\hbar\gamma = 0.123$ eV, $\hbar\omega_0 = 1.58$ eV, $\hbar\gamma_0 = 0.5$ eV and $G_0 = 13$. (b) ε_{Al} considering only Drude part ($G_0 = 0$). 4

2.2 (a) Band structure of Al. The black arrows show the bands resposible for the interband transitions. Figure from [3]. (b) Al nanodisk used as a plasmonic nanoresonator (c) Al asymmetric microcavity used as a perfect absorber. 5

3.1 Cavity-emitter coupling regimes depicted in the energy dependence on the detuning, $\delta = \omega_c - \omega_0$. (a) **Uncoupled**: no interaction between the energy levels. The emitter decays spontaneously. (b) **Weak coupling**: energy levels slightly change, but no mode splitting is resolvable. The emission rate is modified by the cavity optical density modes (Purcell effect). (c) **Strong coupling**: new energy levels of the hybrid system are generated, giving rise to an anticrossing in energy of $\hbar\Omega_R$. The spontaneous emission becomes reversible, such energy transfer between them occurs at a frequency Ω_R. 10

4.1 (a) Schema of Transfer Matrix Method (TMM). The interface and propagation matrices are depicted for i and $j-$th layers. (b) Stack used in the experiments and in calculations. 16

4.2 Electron beam lithography process steps. (a) The substrate with positive resist on top is exposed to the electron beam in a designed pattern. (b) The exposed resist is developed, giving rise to holes in the resist (c) 20 nm of Al is deposited by e-beam evaporation to generate disks and (d) during the lift-off the rest of the resist is washed away. . 18

4.3 Hole-Mask colloidal Lithography (HCL) fabrication process flow. (a) Spin coating of 240 nm of PMMA, followed by reactive oxygen plasma treatment for 5 s at 50 W. (b) Formation of a self-organized layer of PS beads on the surface by using a positively charged monolayer of PDDA. (c) Deposition of Cr to form the metallic mask. (d) Removal the PS beads to uncover the holes of the mask by tape-stripping. (e) Oxygen plasma etching to create the cylinders in the mask. (f) Al e-beam evaporation to form the disks. (g) Lift-off in acetone. 19

4.4 Images of the obtained nanodisks by HCL and EBL. (a) SEM of HCL nanodisks of 172 nm of diameter and 20 nm height. (b) SEM of HCL nanodisks of 200 nm of diameter and 20 nm height. (c) Dark-field optical image of an array of 20 nm height Al nanodisks fabricated by EBL, the diameter increases from 170 nm (leftmost) to 230 nm (rightmost). (d) SEM of EBL nanodisk, with 20 nm height and a diameter of 230 nm. (e) Image of the EBL array scattering spectra reconstructed using hyperspectral imaging technique. 20

4.5 Optical characterization of Al nanodisks (a) Working principle of extinction measurements with a spectrophotometer: collimated light is sent to a monochromator (grating and slit) such that the light transmitted through the sample at each wavelength is recorded. (b) Schema of Dark-Field spectroscopy setup: light is sent in large angles through a 100× objective, the scattered light is collected by the objective. The detection can be through a liquid crystal filter (LCF) to record the image of the scattered light at a certain wavelength with a CCD, or through a fiber coupled to a spectrometer. 21

4.6 Schema of the reflection measurements setup of the microcavities. (a) Normal incidence. Light is sent and collected at normal incidence and detected by fiber-coupled spectrometer. (b) Dispersion measurements. The microscope is used in back focal plane (BFP) detection, with a very high NA objective (40×, NA= 0.95). Spectra was taken for 4 different points along the black dotted line in the BFP. 24

5.1 Calculated extinction efficiency (Q_{ext}) of Al nanodisks. The disks are 10 nm in height and a diameter of (a) 80 nm, such that LSPR is far from Al IBTs, and (b) 200 nm to obtain an overlap of LSPR and IBTs. (c) Uncoupled cavity mode of a nanodisk with d=200 nm and h=10 nm when changing the refractive index of the surroundings. (d) Anticrossing of the cavity mode (on the left) and the IBTs (in blue). . 26

5.2 Coupled Oscillator Model fitting to Q_{ext} spectra calculated using DL model. (a) Example of the fitted spectra for a disk of d=200 nm, h=10 nm and $n = 1.25$. Anticrossing between IBTs and LSPR with the maximum of the DL and COM spectra highlighted. The anticrossing is obtained by varying: (b) n of a disk of d=200 nm and h=10 nm, (c) diameter of a disk of h=10 nm with $n = 1.25$ and (d) height of a disk of d=200 nm and $n = 1.25$. The variation in g is shown as an inset in each plot. 28

5.3 (a-c) Extinction measurements of Al nanodisks fabricated by HCL. The extinction for different heights is shown with an offset in each plot. (d-f) Extinction calculations using MLWA to fit the experimental data. Made considering a low quality Al ($G_0 = 5.2$). The Drude spectra is shown in dotted lines. (g-i) Extinction calculations using the Coupled Oscillator Model for a given coupling strength. The first column from left to right shows the results for nanodisks of d=172 nm, the second column shows results of the same nanodisks covered in PMMA and the third column has d=200 nm. 30

5.4 Coupled Oscillator Model (COM) fit of Q_{ext} spectra calculated using DL model with $G_0 = 5.2$. (a) Variation in diameter with $h = 10$ nm and $n = 1.25$. (b) Variation in height for a disk of $d = 200$ nm and $n = 1.25$. The insets show the values of g for the COM. 31

5.5 Hyperspectral imaging technique measurements for Al deposited at (a) 1-2 Å/s and (b) 20 Å/s. (c) Calculations of the scattering cross section considering a low quality Al ($G_0 = 5.2$). (d) Spectra of nanodisks deposited at 20 Å/s done by fiber coupled to a spectrometer. Note that the scale of the axis is different for each plot. 32

5.6 Reflectivity calculations of the asymmetric cavities by TMM. (a) R for a 100 nm thick Al bottom mirror. (b) R of the mirror with a 200 nm thick layer of SiO_2 on top, $n = 1.45$. (c) R for a cavity with $t = 5$ nm for the top mirror, considering ε_{Drude}. (d) Cavity with $t = 5$ nm and the full DL model, with $G_0 = 13$. (e) Uncoupled cavity mode depending on the spacer thickness, d ($G_0 = 0$). (f) R dependence on d with IBTs ($G_0 = 13$). The uncoupled components are shown in dashed lines. 34

5.7 (a) Calculations for different spacer thickness, d, with $t = 5$ nm and $G_0 = 5.2$ (b) Normal incidence reflection measurements of asymmetric microcavities ($Al(5)/SiO_2(d)/Al(100)$) for different d. (c) Dispersion measurements of a microcavity with $d = 225$ nm and $t = 5$ nm. 36

5.8 R calculations for cavities with a $h = 20$ nm layer of molecules resonating in $\hbar\omega_{mol} = 1.58$ eV on the top. (a) R for a 100 nm thick Al bottom mirror. (b) R of the mirror with a 200 nm thick layer of SiO_2 on top, $n = 1.45$. (c) R for a cavity with $t = 5$ nm for the top mirror, considering ε_{Drude}. (d) Cavity with $t = 5$ nm and the full DL model, with $G_0 = 13$. (e) Cavity mode depending on the spacer thickness, d ($G_0 = 0$), with molecules on top ($h = 20$ nm). (f) R dependence on d with IBTs ($G_0 = 13$) and a 20 nm layer of molecules on top. The uncoupled components are shown in dashed lines. 37

5.9 (a) Reflectivity of a 70 nm thick layer of molecules on top of the cavity (b) R for molecules ($h = 20$ nm) on top of the cavity with IBTs. (c) Variation of the Rabi splitting ($\delta = 0$ m for $d = 218$ nm) with the thickness of the layer of molecules. 38

5.10 Reflectivity calculations for different stacks considering WSe_2 on top of the cavity. The spacer thickness is $d = 200$ nm and the WSe_2 thickness is $h = 8$ nm. Left column: calculations using ε_{WSe_2} obtained by fitting a single lorentzian to the A-exciton (a). Right column: calculations with the ε_{WSe_2} for the bulk material (b). R for the bare WSe_2 is shown in (c) and (g). R for WSe_2 on top of the spacer is shown in (d) and (h), a cavity mode appears around 500 nm, which can interact with the B-exciton. Then WSe_2 on top of the cavity without IBTs is shown in (e) and (i). The 3-component system is shown in (f) and (j). 39
5.11 Left column: Reflectivity calculations using ε of A-exciton Lorentz fit. Right column: calculations using ε_{WSe_2}. (a-b) WSe_2 thickness variation on top of the bottom mirror. (c-d) Variation in spacer thickness, for $h = 8$ nm, considering only Drude for Al. (e-f) Spacer thickness variation for $h = 8$ nm, considering also IBTs contribution. 40

1
Introduction

Light-matter interactions have allowed us to perceive and study the world. At the core of these interactions is the absorption or emission of a photon by an electronic transition. Thus, the interaction has been studied through a single two level system (such as an atom) and an optical cavity by quantum optics. Such studies have been extended to different kinds of transitions (emitters) and to ensembles of particles, such as molecules or excitons in 2D materials [4].

There are two main regimes of light-matter interactions: *weak* (*Purcell*) regime and the *strong* coupling regime. The coupling regime in which a certain system is found depends on the coupling strength, g, between the components. The coupling strength is a measure of the rate at which both components exchange energy between them. It depends directly on the dipole moment of the transition and inversely on the mode volume of the cavity.

When g is small, the energy is mainly transferred from one component to the other. This is called Purcell or weak coupling regime, in which the emission rate of the emitter is modified due to the presence of the cavity.

In the case of g being larger than the average dissipation rates i the system, the energy transfer between the components becomes reversible. Then, energy will oscillate from one component to the other in what are called *Rabi oscillations*. This regime is called *strong coupling* regime [5, 6].

A strongly-coupled system is a hybrid where the newly formed quasiparticles, called *polaritons*, have properties of both light and matter. Thus, polaritons are a way of increasing photon-photon interaction, and the bosonic part of a polariton can be used for lasing or condensation of originally fermionic systems [4].

Additionally, it has recently been shown that some material properties are affected by strong coupling, such as charge transport and chemical reactivity [7, 8, 6]. Opening new opportunities to tailor material properties. Another application for strongly-coupled systems is on quantum information processing, because Rabi oscillations are a coherent process.

The problem is that most cavities are closed, meaning that the emitter is physically between two mirrors, which hinders the applicability of strongly-coupled systems. Therefore, it is important to look for open cavities as platforms for strong coupling. For this purpose, part of the strong coupling community now uses plasmonic nanoresonators [5].

Plasmonic nanoresonators have allowed to manipulate light at the nanoscale. They behave as a sub-diffraction wavelength resonator due to the collective oscillations of free electrons in metals, which are called *localized surface plasmon resonances* (LSPR). Even though, being a metallic system increases dissipation, the

poor quality of the cavity is compensated by nanometer scale mode volume [5].

The objective of this work was to study the coupling between interband transitions of Al and light. Two different types of Al cavities where used: plasmonic nanoresonators and asymmetric metallic microcavities.

This is a peculiar system to study because the cavity is coupled to an intrinsic transition of the material that composes it. In a sense, the cavity is coupled to itself. Therefore, an important highlight of this work is the simplicity of the samples where light-matter interaction can be studied.

Furthermore, as mentioned before, it is necessary to find a platform with an open cavity for strong coupling. The asymmetric microcavity studied here has potential for such purpose. Experiments will be performed to test its applicability soon, as described by the end of this thesis. However, they are outside the scope of this work.

1.1 Thesis outline

To understand the importance of the results of this work, the thesis is structured in the following way. In the beginning, chapter 2 presents the uncoupled characteristics of the system: optical properties of metals, the interband transitions (IBTs) in Al and the two types of cavities. Thus, the chapter focuses on the two ingredients that will compose the coupled system. Throughout this thesis, the nanodisks are discussed before the microcavities.

An important concept to highlight in section 2.1 is the Drude-Lorentz model of the dielectric function, since it is used in all the calculations in this work. Once the dielectric function is introduced, a description of the two types of cavities used to study light-IBTs interaction is given in section 2.2. The theory presented there was used for the calculations of both systems.

This is followed by chapter 3, which focuses on the interaction of both ingredients. It presents an explanation on the different light-matter regimes, the characteristics of strong coupling, and the previous studies regarding light-IBT interactions. Likewise, it includes a description of the coupled oscillator model, that was used to calculate the coupling strength, g.

The methods used in this work are described in chapter 4. Including the calculations made in both types of cavities. Also, the fabrication process of Al nanodisks and microcavities. Lastly, the optical characterization of the samples is explained.

Chapter 5 contains the results obtained in this work and it is divided in two sections. On the one hand, section 5.1 covers IBT-LSPR coupling in Al nanodisks. On the other hand, section 5.2 describes the results obtained for the asymmetric microcavities. Both sections contain the information given by calculations first and the experimental measurements after. Every section is closed by a brief summary of the important points discussed to facilitate comprehension of the main results of the full work.

Finally, chapter 6 gives an overview of the main results, discusses the encountered problems and some ideas to overcome them, as well as perspectives and ideas for future work, closing with a general conclusion.

2

On light and matter

This chapter is devoted to the properties of interband transitions (IBTs) in Aluminum (Al) and both cavity modes, in order to study the coupling between them.

First, the dielectric function is described, since it contains the information about the material optical response and is very important to understand the calculations made in this work. This is followed by a brief description of IBTs in Al.

Then the basic theory behind the two different structures to obtain the cavity modes used to couple to the IBTs is covered. Both structures are resonators: Al nanodisks (plasmonic nanoresonators) and asymmetric microcavities with Al mirrors.

2.1 Optical Properties of Metals

The optical properties of metals depend on the response of its bound and free electrons to an external field. Such response is well described by either its complex dielectric function, $\varepsilon = \varepsilon^{'} + i\varepsilon^{''}$, or its complex refractive index, $\mathcal{N} = n + i\kappa$.

To calculate the dielectric function of the metal we can consider a microscopical approach of both the free and bound electrons contributions. Which are well described by Drude and Lorentz model, respectively.

This chapter covers first the Drude-Lorentz model, since it was used for $\varepsilon(\omega)$ in the calculations. The nature of IBTs in Aluminum (Al) is discussed, allowing to understand the choice of such material for this work.

2.1.1 Drude-Lorentz model

The general idea of the Lorentz microscopic model of polarization is to think about bound ions and electrons in a material as harmonic oscillators when the material responds to an applied electric field, $\mathbf{E}(\omega)$. This allows us to calculate the polarization, $\mathbf{P}$ and thus, its dielectric function.

Then, the displacement from the equilibrium position, $\mathbf{x}$, of any oscillator in the material has an equation of motion given by

$$m\ddot{\mathbf{x}} + m\gamma\dot{\mathbf{x}} + m\omega_0^2\mathbf{x} = -e\mathbf{E}_0 e^{-i\omega t}. \tag{2.1}$$

Considering that the applied electric field is light, it oscillates with a given frequency, ω. In contrast to Lorentz model, Drude model for free electrons considers that $\omega_0 = 0$, because there is no restoring force on free electrons in the metal.

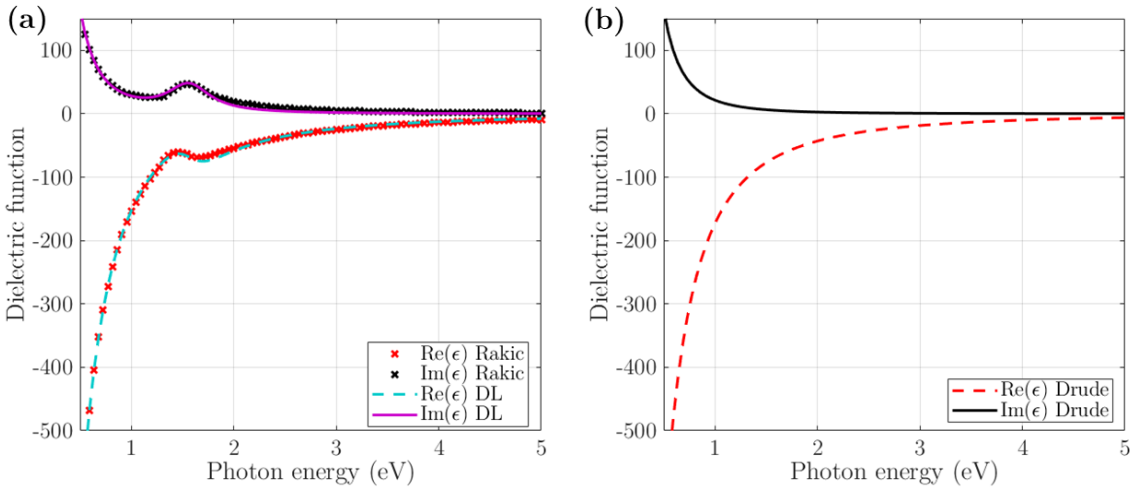

Figure 2.1: *Al dielectric function. (a) Experimental data by Rakic [2] and Drude-Lorentz model fit, with* $\hbar\omega_P = 13.3$ *eV,* $\hbar\gamma = 0.123$ *eV,* $\hbar\omega_0 = 1.58$ *eV,* $\hbar\gamma_0 = 0.5$ *eV and* $G_0 = 13$*. (b)* ε_{Al} *considering only Drude part (*$G_0 = 0$*).*

In such case, by solving equation 2.1 we find that the displacement of each oscillator is

$$\mathbf{x}(\omega) = \frac{e}{m}\frac{\mathbf{E}(\omega)}{\omega^2 + i\gamma\omega}. \tag{2.2}$$

The induced dipole moment of each oscillator is $\mathbf{p} = -e\mathbf{x}$. If there are N oscillators per unit volume, then the total polarization is

$$\mathbf{P} = N\mathbf{p} = -\frac{\omega_P^2}{\omega^2 + i\gamma\omega}\mathbf{E}. \tag{2.3}$$

Where $\omega_P = \left(\frac{Ne^2}{m\varepsilon_0}\right)^{1/2}$ is the plasma frequency of the metal, which depends on the number of free carriers per unit volume N, and their effective mass, m. Given that $\mathbf{D} = \varepsilon(\omega)\varepsilon_0\mathbf{E} = \varepsilon_0\mathbf{E} + \mathbf{P}$, the dielectric function of a Drude metal is

$$\varepsilon_{Drude} = 1 - \frac{\omega_P^2}{\omega^2 + i\gamma\omega}. \tag{2.4}$$

Al dielectric function is well described by Drude model for most of the spectrum, due to its amount of free electrons. The only region where it is not well described is in the near-infrared. There, light absorption by interband transitions (IBTs) should be taken into account [9]. The full dielectric function, that considers both free and bound electrons, is then $\varepsilon(\omega) = \varepsilon_{Drude} + \varepsilon_{IBT}$.

For Al IBTs, the solution of equation 2.1 is very similar to 2.2, but with the restoring force different from zero, meaning that ω_0 has a finite value (Lorentz model). In which case the full dielectric function is given by

$$\varepsilon(\omega) = 1 - \frac{\omega_P^2}{\omega^2 + i\gamma\omega} + \frac{G_0\omega_0^2}{\omega_0^2 - \omega^2 - i\gamma_0\omega}. \tag{2.5}$$

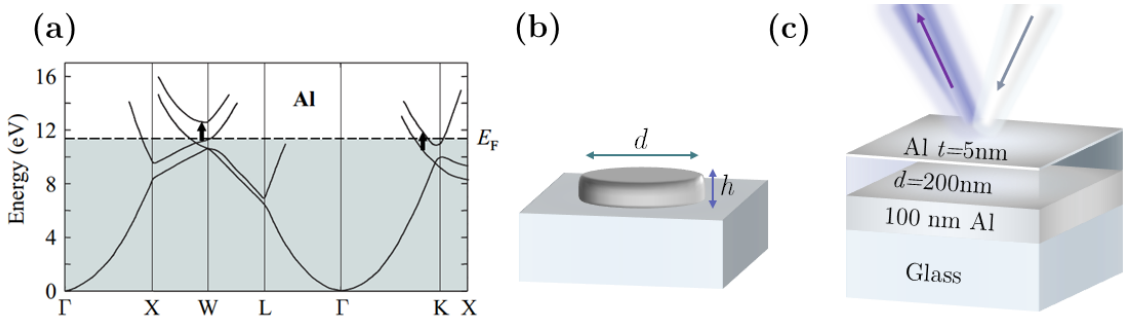

Figure 2.2: *(a) Band structure of Al. The black arrows show the bands resposible for the interband transitions. Figure from [3]. (b) Al nanodisk used as a plasmonic nanoresonator (c) Al asymmetric microcavity used as a perfect absorber.*

It is important to point out that $\omega_P \neq \omega_P^* = \left(\frac{N^* e^2}{m^* \varepsilon_0}\right)^{1/2}$, since the former considers free electrons, whereas the latter is for bound electrons. In equation 2.5 it is assumed that $\omega_P^{*2} = G_0 \omega_0^2$, where G_0 represents the *oscillator strength*, γ_0 the damping, and ω_0 the frequency of the spectrally localized IBTs in Al [10]. Let us note that equation 2.5 is suitable for localized IBTs (as in Al), but it is not the best description for extended IBTs (like in Au).

The measured dielectric function of Al was obtained from literature and it is shown in figure 2.1 [2]. Such experimental data was fitted with Drude-Lorentz model (eq. 2.5), for which $\hbar\omega_P = 13.3$ eV, $\hbar\gamma = 0.123$ eV, $\hbar\omega_0 = 1.58$ eV, $\hbar\gamma_0 = 0.5$ meV and $G_0 = 13$. The fit is shown in figure 2.1(a).

2.1.2 Interband Transitions of Al

Al is a cheap, abundant, and a good conductor metal that has superconducting properties, and more recently, has been considered as a good plasmonic material [11].

Interband transitions (IBTs) are direct transitions of electrons between different bands in the metal due to the absorption of a photon. Those transitions are possible because of the short penetration of the external field into the material. IBTs are responsible for the colours in noble metals such as gold and copper.

As was briefly introduced above, IBTs can be broadly extended or localized in a specific energy range depending on the material. Some of the metals in which they are localized are nickel (Ni), iron (Fe), copper (Cu) and aluminum (Al). For them, IBTs are around 4.7 eV, 2.5 eV, 2.1 eV and 1.5 eV, respectively [10].

In the case of Al, the spectrally localized IBT absorption is due to the *parallel band effect*. In such effect, the absorption probability increases when a band below the Fermi level is approximately parallel to another one above it. This increase is related to Fermi's Golden rule, since many electrons can make the same energy transition the density of states is higher, thus the transition rate is larger. This effect takes place between the bands marked with a black arrow in figure 2.2(b), where the energy difference between the bands is around 1.5 eV [3]. We should remark that these transitions are observed as a peak in $\mathrm{Im}(\varepsilon_{Al})$ as showed in figure 2.1(a).

2.2 Optical Cavity Modes

Two different kind of resonators were used in this work to couple the interband transitions of Al to optical cavity modes. The first one was given by plasmonic resonators (Al nanodisks) and the second by two Al mirrors forming an asymmetric microcavity.

Both resonators are metallic, and therefore are considered highly *lossy*. The *quality factor*, $Q = \omega_c/\gamma_c$, quantifies how lossy a resonator is [12]. Where, ω_c is the resonance frequency and γ_c is the full width at half maximum (FWHM). The latter is a measure of the spectral confinement of the cavity. Intuitively, Q gives an idea of the time the photon is *trapped* inside the cavity before being lost to the environment.

2.2.1 Plasmonic nanoresonators

Metallic nanoparticles can be considered nanoresonators in the sense that light is *bouncing* back and forth inside a nano-sized structure. This subwavelength resonators are possible thanks to the free electrons in the metal that oscillate as response to an external field and are constrained to the nanoparticle size. Those collective oscillations in surface charge densities are called *localized surface plasmon resonances* (LSPR). Moreover, since they are a result of light coupled to the free electrons in the metal, they are polaritons, thus they are also known as *localized surface plasmon-polaritons* (LSPP) [13].

These plasmonic effects are found in materials where the complex dielectric function has a negative real part and the imaginary part is not too large. Reason for which metals are used.

The LSPR has a maximum when the natural frequency of the nanoparticle resonates with the applied field. The resonance frequency depends on the geometry and material of the nanoparticle, as well as the surrounding media. In this study, the geometry is a nanodisk and the material is Al.

LSPR is experimentally characterized by the absorption, scattering or extinction spectra of the nanodisks, because the amount of light that interacts with them has a maximum at the resonance.

2.2.1.1 Scattering by a small oblate ellipsoid

To analytically calculate the scattering and extinction spectra of nanodisks we can model them as oblate spheroids ($a = b < c$). Let us consider small ellipsoids compared to the wavelength, such that $a, b, c \ll \lambda$, embedded in a homogeneous media with a dielectric function ε_d. Due to the long wavelength, the field is considered spatially static for the particle, therefore it is called *quasi-static approximation*.

In such case, the applied field induces a dipole moment outside the particle $\mathbf{p} = \varepsilon_d \alpha \mathbf{E}_0$. With the polarizability, α of the ellipsoid given by

$$\alpha_i(\omega) = \frac{4\pi abc}{3} \frac{\varepsilon(\omega) - \varepsilon_d}{\varepsilon_d - L_i(\varepsilon(\omega) - \varepsilon_d)}. \tag{2.6}$$

Where, $i = \{x, y, z\}$ is the direction of polarization. For an oblate spheroid, the geometric depolarization factor $L_{x,y}$ is given by

$$L_{x,y} = \frac{g(e)}{2e^2}\left[\frac{\pi}{2} - \tan^{-1} g(e)\right] - \frac{g^2(e)}{2}. \tag{2.7}$$

With $g(e) = \left(\frac{1-e^2}{e^2}\right)^{1/2}$ and $e^2 = 1 - \frac{c^2}{a^2}$ [14]. Meaning that the geometrical depolarization factor depends exclusively on the aspect ratio of the ellipsoid.

From equation 2.6 follows that when the real part of the denominator is zero there is a maximum induced dipole moment. The frequency at which it happens defines the LSPR resonance frequency, ω_c.

In the quasi-static approximation, $\alpha(\omega)$ is independent of the nanoparticle size, which is counterintuitive since larger nanoparticles have larger dipole moment, thus they should radiate more. This issue is due to the assumption that the field inside the nanodisk is homogeneous, and because the approximation ignores effects related to retardation and radiation reaction. To solve the problem we can either numerically solve the full electrostatic problem using Mie's Theory, or we can use the modified long wavelength approximation [14, 13].

2.2.1.2 Modified long wavelength approximation

To extend the applicability range of the quasi-static approximation, the modified long wavelength approximation (MLWA) includes two other effects: radiation reaction and dynamic depolarization. The former is given by the fact that the field induced by the dipole reacts on itself. The latter considers that the dipole is oscillating at a finite speed, thus this term includes retardation [15, 13].

To include this terms, a depolarization field is proposed, such that $\mathbf{p}(\omega) = \alpha(\omega)\varepsilon_d(\mathbf{E}_0 + \mathbf{E}_{dep})$. By taking into account $\mathbf{E}_{dep}$ the polarizability is given by

$$\alpha_{MLWA} = \frac{\alpha(\omega)}{1 - \frac{k^2}{4\pi a}\alpha(\omega) - i\frac{k^3}{6\pi}\alpha(\omega)}. \tag{2.8}$$

The polarizability $\alpha(\omega)$ was given in equation 2.6. The second term in the denominator of eq. 2.8 is given by the dynamic depolarization and it is responsible for the redshift of the resonance frequency, ω_{PL}, with the increase of particle's volume. The third term in the denominator is the radiation damping correction. It broadens the resonance peak and decreases its magnitude for larger nanoparticles.

Strictly speaking the MLWA is valid for diameters up to ~ 100 nm, but experimentally it has shown good agreement with nanodisks up to ~ 500 nm [16]. MLWA is limited because it does not include high-order multipole terms nor the retardation of the exciting field across the particle [15].

Cross sections for extinction (σ_{ext}) and scattering (σ_{sca}) are defined to quantify the amount of light interacting with the nanodisk [14].

$$\begin{cases} \sigma_{sca} = \frac{k^4}{6\pi}|\alpha_{MLWA}|^2, \\ \sigma_{ext} = k\,\mathrm{Im}(\alpha_{MLWA}). \end{cases} \tag{2.9}$$

Both quantities can be measured and compared to the calculated ones via the extinction and scattering efficiency. They are dimensionless parameters given by $Q_{sca,ext} = \sigma_{sca,ext}/(\pi r^2)$. Where, r is the ratio of the particle.

2.2.2 Asymmetric microcavities

A microcavity consists of two reflecting surfaces separated by a transparent dielectric media (spacer) which is usually a few micrometers thick (fig. 2.2(c)). Then, light will be reflected from each mirror, allowing to trap it between them.

Moreover, the phase shift in every round-trip generates interference. This creates a resonance condition for the microcavity that depends on the distance between the mirrors. Thus, the wavelength of the trapped light depends on that distance. Also, the time during which the light is trapped depends on the reflectivity of the mirrors, determining its quality factor, Q.

The best known resonator of this type is a Fabry-Pérot resonator, which has both mirrors with equal reflectivity, R. In that case there is a peak in transmission for a wavelength $\lambda_m = 2nL/m$. Where m is the order of the mode, n is the refractive index of the medium between the mirrors and L the distance between the two perfect mirrors [17].

By breaking the symmetry of the mirrors, such that one of them is very thin, it is possible to get a perfect absorber configuration based on the same concept as Salisbury screens, which were developed for radars. The idea is similar to anti-reflection coatings, and have been used in a metal-insulator-metal structure to absorb certain frequencies of light [18].

The general idea of a Salisbury screen is based on destructive interference of the incoming wave using a metal-insulator-metal structure such as the one depicted in figure 2.2(c). The structure is such that a top thin mirror partially reflects the incoming wave, the rest is transmitted and travels through a spacer of a thickness $\sim \lambda m/4$. Where m is the order of the mode. Then the wave is reflected by a bottom perfect reflector, such that there is a total π phase shift with respect to the wave reflected in the top mirror. Hence, the destructive interference cancels reflection for that wavelength, λ.

Given that the bottom mirror is a perfect reflector, the lack of reflection of the full system means that the light is perfectly absorbed.

In fact, the dielectric layer is transparent and will not absorb much of the light power. The absorbed power has been shown to be stronger in both metal-dielectric interfaces inside the cavity [18].

In this work, the perfect absorption in asymmetric cavities was used to enhance the absorption of light in the top mirror of an Al microcavity (fig. 2.2(c)).

3

Light-Matter coupling

This chapter is dedicated to the coupling between light and matter. In particular to IBT-light coupling. To begin, the characteristics of weak and strong interaction regimes are described. Then, there is a discussion on the importance and advantages of strongly coupled systems.

This is followed by a fully classical description of strongly coupled systems. Such description was used to calculate the coupling strength of LSPR-IBT interaction in Al nanodisk.

Finally, a description of previous works related to the interactions between the interband transitions (IBTs) and LSPR is given.

3.1 Basics on weak and strong coupling

The most studied system of light-matter interaction is a two-level system (TLS) inside a perfect cavity where a photon is *bouncing back and forth*. The dynamics of this system is described by Jaynes-Cummings Hamiltonian. This is a very simplified picture, hard to achieve experimentally. Nonetheless, the theory is robust enough to be able to describe the system with an emitter instead of a TLSs. Hence, it has become the working horse in quantum optics and quantum information [19].

To facilitate the comparison between theoretical and experimental results it is even possible to include dissipation in the cavity (γ_c), and the emitter (γ_0) in the Hamiltonian [4].

$$H_{loss} = \hbar \begin{bmatrix} \omega_0 - i\gamma_0/2 & g \\ g & \omega_c - i\gamma_c/2 \end{bmatrix}. \tag{3.1}$$

Where $g = (\mathbf{d} \cdot \mathcal{E})/\hbar$ is the *coupling strength*, which is a measure of the interaction rate between the emitter and the cavity. This parameter depends on the transition dipole moment of the emitter ($\mathbf{d}$) and the vacuum field in the resonator at the emitter position, $\mathcal{E}$. The latter increases when decreasing the mode volume of the cavity as $\mathcal{E} \propto 1/\sqrt{V}$.

When g is small in comparison with the decay rate of the uncoupled components, we say that the emitter interacts *weakly* with the cavity, In that case, if $g > \gamma_0$ the spontaneous emission rate is modified due to the change of optical density of states and Fermi's golden rule, which gives rise to Purcell Effect. This effect allows to tailor the decay rate of emitters, to either enhance their emission or protect them from decaying to the environment [20].

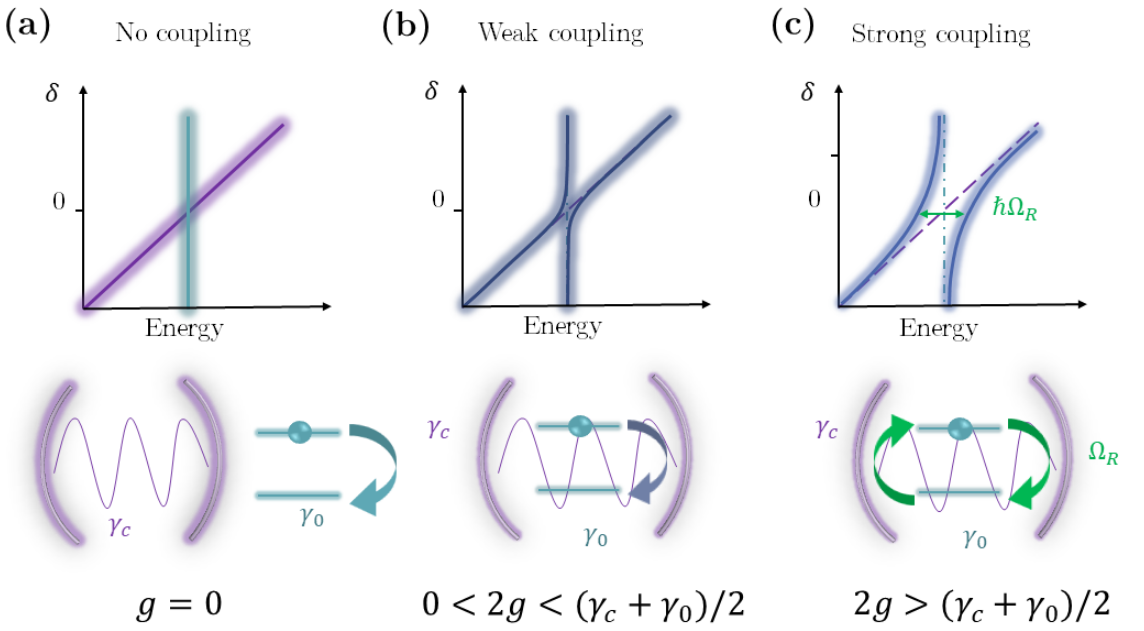

Figure 3.1: *Cavity-emitter coupling regimes depicted in the energy dependence on the detuning, $\delta = \omega_c - \omega_0$. (a)* ***Uncoupled****: no interaction between the energy levels. The emitter decays spontaneously. (b)* ***Weak coupling****: energy levels slightly change, but no mode splitting is resolvable. The emission rate is modified by the cavity optical density modes (Purcell effect). (c)* ***Strong coupling****: new energy levels of the hybrid system are generated, giving rise to an anticrossing in energy of $\hbar\Omega_R$. The spontaneous emission becomes reversible, such energy transfer between them occurs at a frequency Ω_R.*

The coupling strength can increase by increasing **d** or decreasing V. If the interaction between the emitter and the cavity is strong enough, the energy will bounce back and forth between the cavity and the emitter before it is dissipated to the environment. At this point, spontaneous emission becomes reversible and the observed energy oscillations between the emitter and the cavity are called *Rabi oscillations*. This interaction is then considered in the *strong coupling regime*.

It is a very interesting regime because both systems (light and matter) are interacting so strongly that it is not possible to distinguish them, they become a hybrid. Then, the new system forms new energy levels (similar to the bonding and anti-bonding energies of small molecules), which leads to an avoided crossing in the energy when the detuning of both frequencies comes close to zero, $\delta = \omega_c - \omega_0 \approx 0$ (fig. 3.1).

The new frequencies related to the energy levels of the hybrid system depend on the dissipation rates of the uncoupled systems and its original frequencies, as follows,

$$\omega_\pm = \frac{\omega_0 + \omega_c}{2} - \frac{i}{4}(\gamma_0 + \gamma_c) \pm \sqrt{g^2 + \frac{1}{4}\left(\delta - i\frac{(\gamma_0 - \gamma_c)}{2}\right)^2}. \tag{3.2}$$

The *Rabi splitting* between the two states, Ω_R, is given at the resonant condi-

tion, $\delta = 0$. In this case the excitation is delocalized evenly between the cavity and the emitter, creating a hybrid.

$$\Omega_R = \sqrt{4g^2 - \left(\frac{\gamma_0 - \gamma_c}{2}\right)^2}. \tag{3.3}$$

Moreover, while the system remains hybridized the interaction is coherent, making it a very interesting regime for quantum information processing and control. Also, the new hybrid has characteristics of both light and matter, giving the new system mixed bosonic and fermionic characteristics. This can be used to tailor material properties to enhance exciton transport, to look for polariton condensates and lasing, to change chemical reactivity, etc [4, 7, 6].

In fact, it has been shown that strong coupling modifies the work function of molecules [8]. Also, there are theoretical studies to determine how much can the molecular structure be changed when it is strongly coupled to a cavity [21].

3.1.1 The advantage of lossy cavities

Most of the strongly coupled systems have been achieved with high quality factor (Q) cavities, such that the photons are trapped in the cavity for a long time, increasing the chances of interaction with the emitter.

Nevertheless, from equation 3.3 it is deduced that the splitting will only be real when $2g > |\gamma_0 - \gamma_c|/2$. Meaning that strong coupling can be achieved for a smaller g when both components have similar dissipation rates.

Of course, having $\gamma_0 \sim \gamma_c$ is not enough to observe strong coupling. We can consider that a system is strongly coupled when both hybrid modes are resolvable and when the Rabi splitting is larger than the average dissipation rate of each component, $\Omega_R > (\gamma_0 + \gamma_c)/2$ [5, 4].

There are some emitters with very narrow linewidths (as single atoms or quantum dots) which can strongly couple to high Q cavities. However, when trying to couple to emitters with broader linewidth (as some molecules) lossy cavities are useful. In fact, lossy plasmonic nanoresonators have allowed to control the plasmon-emitter strong coupling at room temperature and with open cavities [22, 5, 23].

For this study, IBTs of Al are very broad ($\gamma_0 \sim 500$ meV), and working with metallic systems give us cavity mode linewidths, γ_c, of the same order for both nanodisks and microcavities.

3.2 Classical Coupled Oscillator Model

Light-matter interactions can be understood in several levels, from a fully classical perspective, to a semiclassical, and even in a fully quantum mechanical picture [5]. In this particular case, the simplest description of the IBT-light interaction is fully classical. This picture was described first by Novotny [24]. Interestingly, that picture was developed after the semiclassical and fully quantum mechanical theories were broadly used by quantum opticians [19].

Here is presented a slightly different approach but with the same core idea, it is called the Coupled Oscillator Model (COM).

Let us think about two classical coupled oscillators: one given for the optical cavity and one for the IBTs, or any other emitter. Their displacements from the equilibrium position are given by x_c and x_0, respectively. The oscillators resonate at ω_c and ω_0 and each oscillator has a dissipation term γ_c and γ_0. The coupling strength between them is g. Then, the equations of motion under a driving force field in the cavity, F_c, are given by,

$$\begin{cases} \ddot{x}_c + \gamma_c \dot{x}_c + \omega_c^2 x_c + g\dot{x}_0 = F_c, \\ \ddot{x}_0 + \gamma_0 \dot{x}_0 + \omega_0^2 x_0 - g\dot{x}_c = 0. \end{cases} \tag{3.4}$$

By considering that the solutions must be of the form $x = x_0 e^{-iwt}$, the solutions in frequency space are

$$\begin{cases} x_c = \dfrac{(\omega^2 - \omega_0^2 + i\omega\gamma_0)F_c}{(\omega^2 - \omega_0^2 + i\omega\gamma_0)(\omega^2 - \omega_c^2 + i\omega\gamma_c) - g^2\omega^2}, \\ x_0 = \dfrac{i\omega g x_c}{\omega^2 - \omega_0^2 + i\omega\gamma_0}. \end{cases} \tag{3.5}$$

Now we can relate the displacement of the coupled cavity, x_c to the scattering cross section by the equation 2.9:

$$\begin{cases} \sigma_{sca} \sim \omega^4 |x_c|^2, \\ \sigma_{ext} \sim \omega \,\mathrm{Im}(x_c). \end{cases} \tag{3.6}$$

This simple picture allows us to estimate the coupling strength g between the cavity and IBTs, by fitting the experimental data with the spectra given by equations 3.6.

Let us note that Drude-Lorentz model is very similar to this approach. But here we are considering only two macroscopic oscillators, which interact in a very simple way through g. Whereas Drude-Lorentz model assumes N microresonators per unit area and the interaction is expressed in a less trivial way through the polarizability, $\alpha(\omega)$. Yet, both descriptions are fully classical.

However, the COM is useful in this case because it allows us to calculate g for our system, which is closely related to the g in the Hamiltonian mentioned above (eq. 3.1). Thus, giving us an idea of the Rabi splitting in our system.

3.3 Previously on IBT-light coupling

As mentioned above, light-matter interactions are usually studied in structures with two different entities: a cavity, and an emitter. For this work the interband transitions (IBTs) of Al are considered as the two level system (emitter) to which we couple light. This system is peculiar because the cavity is coupled to an intrinsic transition in the material that composes it. Thus in some way, the cavity is coupled to itself.

IBTs have been usually considered undesired relaxation mechanisms, since they introduce additional dissipative channels for plasmon resonances. Therefore, nanoantennas are usually designed such that the LSPR avoids the interband regions of the metals.

Nevertheless, it has been shown that the interaction of LSPR with extended IBTs results in a Fano-type resonance [25]. Also, the interaction of the LSPR with spectrally localized IBTs has been addressed theoretically by Pakizeh [26] using Drude-Lorentz model (eq. 2.5). In that case the interaction was treated in quasi-static theory, as a dipole-dipole interaction that resulted in two hybrid modes.

The aforementioned study triggered a few experimental works considering spectrally localized IBT-light interactions. The first one, observed for the first time LSPR-IBT anticrossing, by using a nanohole array fabricated by colloidal lithography [27].

Similarly, Lercarme et al., studied the interaction in Al nanorods [9]. They considered that the interaction was analogous to the system LSPR-J-aggregates that is usually studied for strong-coupling, but made no calculations to check if it was indeed strongly coupled.

Finally, another study was conducted by Pirzadeh et al, using Nickel [10]. The coupling was studied in Ni nanodisks fabricated by Hole-mask colloidal lithography (HCL). In their study they observed an energy split of 1.1 eV, used a classical model of strong coupling [24] to explain the mode splitting, and claimed that the two new modes were too wide for the system to be considered in strong coupling.

The difference between Ni and Al is that the IBTs are around 4.5 eV, which is far in the UV, representing a challenge for measurements in normal microscope objectives due to UV light absorption in lenses and objectives.

In short, light-IBT interaction has been studied before using plasmonic nanoresonators. Regarding microcavities, to my knowledge light-IBT interaction has not been addressed in asymmetric microcavities as perfect absorbers, even though symmetric microcavities are broadly used by the strong coupling community [4, 20].

4
Methods

This chapter consists of the description of the methods for calculations, fabrication, and optical measurements of the aforementioned structures.

The theory behind the calculations of the cavity modes was covered in section 2.2. The specifics regarding the calculations of the extinction spectra of the nanodisks and the Transfer Matrix Method (TMM), used for the microcavities configuration, are explained here.

This is followed by the description of the fabrication process of the nanodisks for ensemble and single particle measurements. As well as the microcavities fabrication.

Finally, the experimental setups used for the optical characterization of the samples are depicted. Ensemble measurements were done with spectrophotometry, and different setups in upright and inverted microscopes were used for single particles and microcavities measurements.

4.1 Calculations

4.1.1 Extinction spectra of Al nanodisks

Analytical calculations of extinction and scattering efficiencies for Al nanodisks were made in the quasi-static regime and MLWA using equations 2.9. For that, the disks were assumed to be oblate ellipsoids surrounded by a homogeneous media, such that the polarizability given by (eq. 2.8) is used for the calculations. The theory behind the calculations was described in subsections 2.2.1.1 and 2.2.1.2. It is important to notice that they are spectra originating from light interacting with a single nanodisk, so no interaction between neighboring nanodisks is considered.

The extinction and scattering efficiency were calculated for Al nanodisks of different diameters ($170 - 230$ nm) and heights ($5 - 30$ nm). For the calculations, ε_{Drude} was considered for Al nanodisks *without* IBTs (eq. 2.4). The calculated LSPR resonance with such dielectric function was considered to be the response of the *uncoupled* cavity mode.

After, maintaining the same geometry, the calculations were made for the full dielectric function of Al (shown in equation 2.5). This includes the Lorentz term with $G_0 = 13$, such that the calculations describe the IBT-LSPR interaction in good quality Al. A low quality one was considered with $G_0 = 5.2$, after the experiments were made. This part will be explained in section 5.1.2.

As will be described in the next section, the nanodisks are fabricated on glass

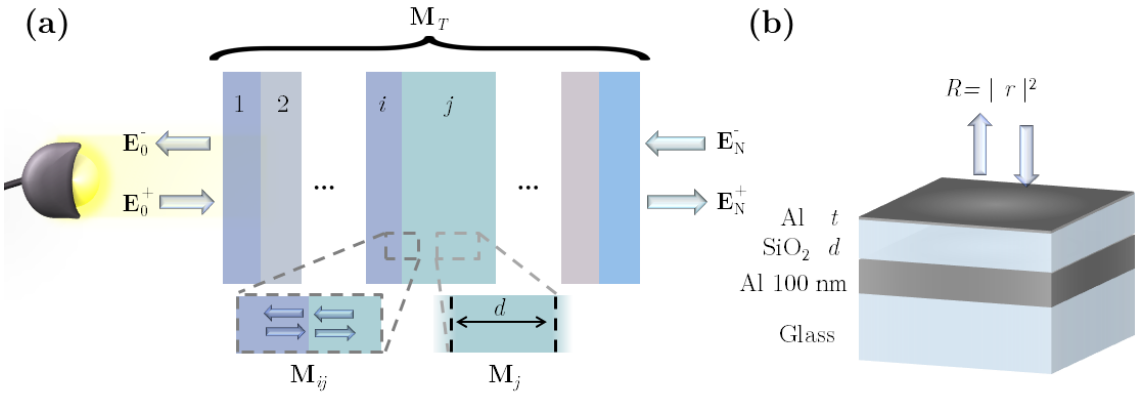

Figure 4.1: *(a) Schema of Transfer Matrix Method (TMM). The interface and propagation matrices are depicted for i and $j-th$ layers. (b) Stack used in the experiments and in calculations.*

substrates, therefore they are not strictly immersed in a homogeneous medium. To take this into account in the calculations, an effective refractive index is considered such that $n_{eff} = \sqrt{(n_{air}^2 + n_{sub}^2)/2}$. Glass refractive index is fixed to 1.45, therefore $n_{eff} = 1.25$. This approximation does not consider the ~ 3 nm self-limiting oxide layer that surrounds the Al nanodisks [11]. In the case of nanoparticles covered by PMMA, the effective refractive index was considered of $n_{eff} = 1.38$.

4.1.2 Transfer Matrix Method

The Transfer Matrix Method (TMM) is a powerful and simple method that allows us to obtain analytically a steady-state solution of the reflected and transmitted light through a multilayered media. To do so it applies the Fresnel equations in the boundaries of each layer and can take into account absorption of the wave through a lossy material [17].

As depicted in figure 4.1, the idea of TMM is to relate the coefficients of the **E** field, in the forward (E^+) and backward direction (E^-), right after the final layer to the ones before the first layer. The relation is given through a total matrix, $\mathbf{M}_T$, that represents the full layered media, such that

$$\begin{bmatrix} E_N^+ \\ E_N^- \end{bmatrix} = \mathbf{M}_T \begin{bmatrix} E_0^+ \\ E_0^- \end{bmatrix}. \tag{4.1}$$

To build the total matrix, it is necessary to multiply every scattering matrix of propagation through every layer ($\mathbf{M}_j$, for the $j-th$ layer) and interface ($\mathbf{M}_{ij}$, for the interface between layers i and j). In general TMM, as Fresnel equations, are polarization dependent. Calculations in this work were done for normal incidence, in which case the equations are the same for both s and p polarization and the matrix for propagation for a distance d through an homogeneous media is given by

$$\mathbf{M}_j = \begin{bmatrix} e^{-ink_0 d} & 0 \\ 0 & e^{ink_0 d} \end{bmatrix}. \tag{4.2}$$

Let us note that the refractive index, n, can be complex. Therefore, the wave damping through a lossy media is taken into account. Additionally, the matrix propagation through an interface is given by

$$\mathbf{M}_{ij} = \frac{1}{2n_j}\begin{bmatrix} n_j + n_i & n_j - n_i \\ n_j - n_i & n_j + n_i \end{bmatrix}. \tag{4.3}$$

Finally, the total matrix is found by multiplying the matrices for every layer and interface in the stack

$$\mathbf{M}_T = \mathbf{M}_{N(N-1)}\mathbf{M}_N \ldots \mathbf{M}_1\mathbf{M}_{01}. \tag{4.4}$$

The reflection and transmission coefficients are given by the ratio between reflected and transmitted coefficients of the field through the full stack. This information can be obtained from the total matrix elements, $M_{T_{ij}}$, when the incoming field in the backward direction (starting from the final layer) is zero, $E_N^- = 0$.

$$r = \frac{E_0^-}{E_0^+} = -\frac{M_{T_{21}}}{M_{T_{22}}}, \tag{4.5}$$

$$t = \frac{E_N^+}{E_0^-} = M_{T_{11}} + rM_{T_{12}}. \tag{4.6}$$

The stack of layers used in this work for the microcavities is shown in figure 4.1(b). In this case $t = 0$, since it includes a perfect bottom mirror. Thus, in this case only the reflectivity of the film stack was calculated, which is given by $R = |r|^2$. For calculations, the refractive index for the glass substrate and the dielectric spacer layer was fixed to $n_s = 1.45$.

The complex refractive index of Al was calculated from the dielectric function fitted by Drude-Lorentz model (eq. 2.5). Which considers IBT-cavity mode interaction. The cavity mode of the uncoupled cavity was calculated by using only the Drude part (eq. 2.4) of the Al dielectric function. This was thought to consider the geometrical configuration with perfect mirrors without IBTs. This was the only possible way to separate both IBTs and cavity mode, since experimentally it is not possible to obtain Al without IBTs.

4.2 Sample Fabrication

As mentioned before, light-matter interactions have been realized in several structures with various kinds of cavities and emitters. This work focused on the interaction of Al IBTs in simple structures, such as bare nanoparticles and metallic microcavities. This section describes the fabrication methods of Al nanodisks and asymmetric microcavities designed for this interaction to be studied.

All the samples of both structures were fabricated on 170 μm thick glass coverslips (Deckglaser #1). Thus, the cleaning procedure for all the substrates was the same. It consisted of 15 minutes in an acetone ultrasonic bath at 100 KHz and 55°C. The same bath was repeated for isopropanol (IPA). Finally, the coverslips were dried with nitrogen gas.

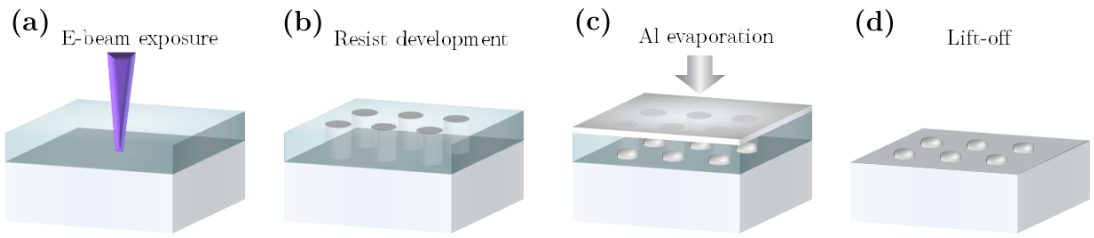

Figure 4.2: *Electron beam lithography process steps. (a) The substrate with positive resist on top is exposed to the electron beam in a designed pattern. (b) The exposed resist is developed, giving rise to holes in the resist (c) 20 nm of Al is deposited by e-beam evaporation to generate disks and (d) during the lift-off the rest of the resist is washed away.*

4.2.1 Nanodisks fabrication

Two different lithographic techniques were used to fabricate Al nanodisks: Electron-beam lithography (EBL) and Hole-Mask Colloidal Lithography (HCL). HCL allows to cover large areas with nanodisks randomly located and EBL was used for single particle fabrication. Even though ensemble nanodisks were fabricated first by HCL and arrays of single particles by EBL later, for clarity reasons, the procedure to make single particles by EBL is described before the HCL process.

4.2.1.1 Electron beam Lithography

Single Al particles were fabricated by EBL on glass by following the process depicted in figure 4.2. After the glass was cleaned, a positive resist (PolyMethyl-Methacrylate - PMMA) was spin coated on top and baked at 180°C for 5 minutes. Then, the resist was exposed to the electron beam with a pattern that consisted of holes arranged in equally spaced rows and columns as shown in fig. 4.4(c). Followed by resist development so that the cylinders are formed in the resist. A 20 nm layer of Al was evaporated on top with two different deposition rates: 1- 2 Å/ and 20 Å/s (e-beam evaporator Lesker PVD 225). The last step was lift-off in acetone, to wash away the resist and uncover the nanodisks.

The nanodisks were fabricated in an array of 7 columns and 9 rows equally spaced by 5 µm, as shown in the optical image of the array (fig. 4.4(c)). The diameter of the nanodisks increases from 170 to 230 nm from the leftmost column to the rightmost one. All the rows are the same for reproducibility tests.

The final shape of the nanodisks was checked by scanning probe microscopy (SEM) to make sure it was correct before the optical characterization. A representative SEM image of a disk with a diameter of 230 nm and 20 nm height is shown in figure 4.4(d).

EBL allows us to fabricate any kind of structure, in particular single particles. Nevertheless, it is a slow process and an expensive tool, thus it is not the most suitable approach for large area coverage.

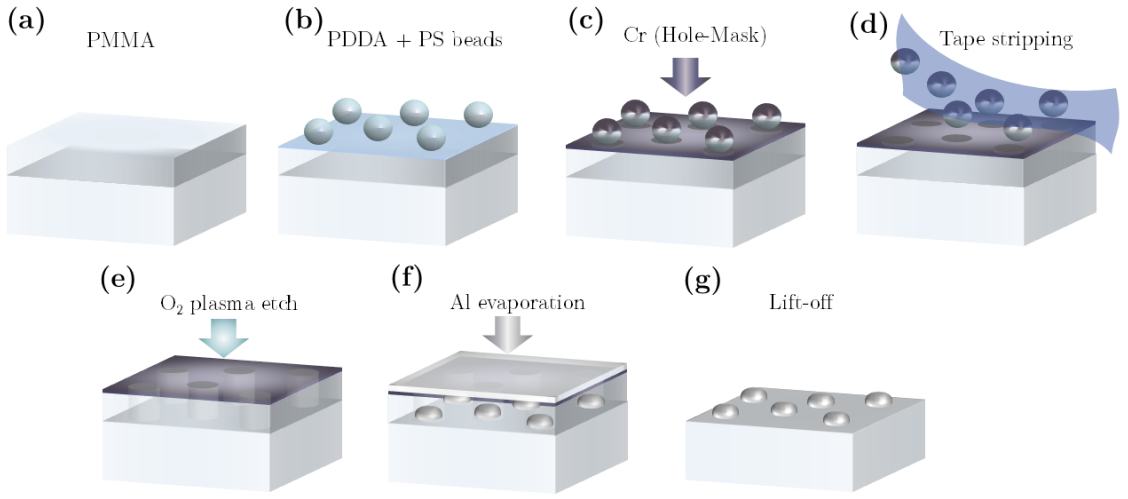

Figure 4.3: *Hole-Mask colloidal Lithography (HCL) fabrication process flow. (a) Spin coating of 240 nm of PMMA, followed by reactive oxygen plasma treatment for 5 s at 50 W. (b) Formation of a self-organized layer of PS beads on the surface by using a positively charged monolayer of PDDA. (c) Deposition of Cr to form the metallic mask. (d) Removal the PS beads to uncover the holes of the mask by tape-stripping. (e) Oxygen plasma etching to create the cylinders in the mask. (f) Al e-beam evaporation to form the disks. (g) Lift-off in acetone.*

4.2.1.2 Hole-Mask Colloidal Lithography

Hole-Mask Colloidal Lithography (HCL) is a method that allows to fabricate nanodisks in large areas by taking advantage of the self-organization of charged silica beads to form a metallic mask on top of the surface [28].

The steps to obtain Al nanodisks are showed in figure 4.3. First, a 240 nm thick layer of (PMMA) is spin coated on top of a clean glass and the samples are baked at 180°C during 5 minutes. This is followed by a reactive oxygen plasma treatment at 50 W for 5 s to make the surface hydrophilic (fig. 4.3(a)).

Then, a monolayer of Poly-(diallyl dimethyl ammonium chloride) (PDDA) is obtained by covering the sample with a solution of 0.2 wt% PDDA during 30 s, rinsing with de-ionized water for 10 s and drying the sample with nitrogen gas. Now a monolayer of polystyrene (PS) beads, with an average diameter of 172 and 200 nm, is formed. To do so, the sample is covered with a 0.1 wt% water suspension of PS beads during 2 minutes, then the sample is rinsed with de-ionized water for 30 s and blown with nitrogen again (fig. 4.3(b)). The positively charged PDDA improves the adhesion of the negatively charged PS beads to the surface and the PS beads will arrange themselves randomly due to electrostatic repulsion between them. Therefore, after this step we obtain a uniform layer of self-organized PS beads.

The next step is to evaporate 10 nm of Cr or Au on top of the beads (e-beam evaporator Lesker PVD 225), depending on the preferred material for the metallic mask (fig. 4.3(c)). In this work Cr was used. The beads will shadow some of the evaporation, leaving holes in the Cr layer underneath them. To uncover the holes, the beads are removed by tape-stripping (fig. 4.3(d)). This will give us a metallic

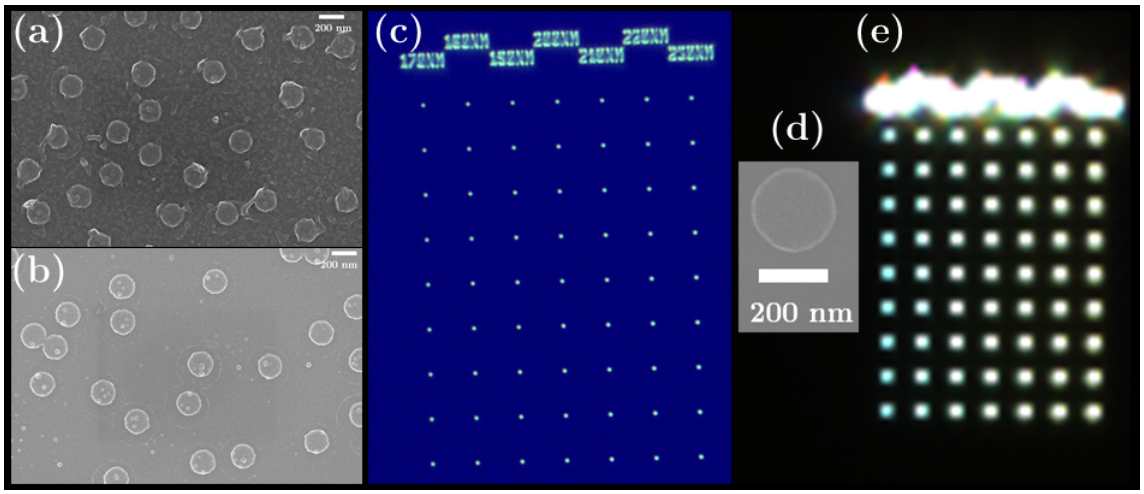

Figure 4.4: *Images of the obtained nanodisks by HCL and EBL. (a) SEM of HCL nanodisks of 172 nm of diameter and 20 nm height. (b) SEM of HCL nanodisks of 200 nm of diameter and 20 nm height. (c) Dark-field optical image of an array of 20 nm height Al nanodisks fabricated by EBL, the diameter increases from 170 nm (leftmost) to 230 nm (rightmost). (d) SEM of EBL nanodisk, with 20 nm height and a diameter of 230 nm. (e) Image of the EBL array scattering spectra reconstructed using hyperspectral imaging technique.*

mask with holes of approximately the same diameter of the beads.

Once the mask is formed, the PMMA is etched with oxygen plasma for 4 minutes at 50 W, through the holes in the mask. (fig. 4.3(e)). This generates a set of openings to the glass substrate. Then the desired height of Al (8, 10, 15, 20, 25 and 30 nm) is evaporated by e-beam evaporation (fig. 4.3(f)). Finally, the PMMA is removed in acetone, along with the upper Al layer. Finishing with nanoparticles randomly distributed of the desired diameter (fig. 4.3(g)).

It is crucial to point out the importance of the e-beam evaporation of the metals in both EBL and HCL methods. Because for them to work it is necessary to deposit the metals with directionality. Therefore, it is possible to create different structures by depositing the metals with different angles. Moreover, the deposition rate and vacuum (should be always below 5×10^{-7} Torr) are very important for the quality of the Al in the nanodisks.

The final HCL structures consisted of Al nanodisks with diameters of 172 and 200 nm, and heights of 8, 10, 15, 20, 25 and 30 nm. The samples were checked with SEM to make sure the diameter and shape were correct. Figures 4.4(a) and (b) show images for 20 nm height HCL nanodisks with diameters of 172 nm and 200 nm, respectively.

4.2.2 Asymmetric microcavities

The samples with the layered structure showed in figure 4.1(b) were fabricated on glass substrates.

Both mirrors were deposited by Sputtering (FHR MS150 Sputter). The thickness of the top mirror was $t = 5, 10$ and 15 nm. The bottom mirror was fixed at 100

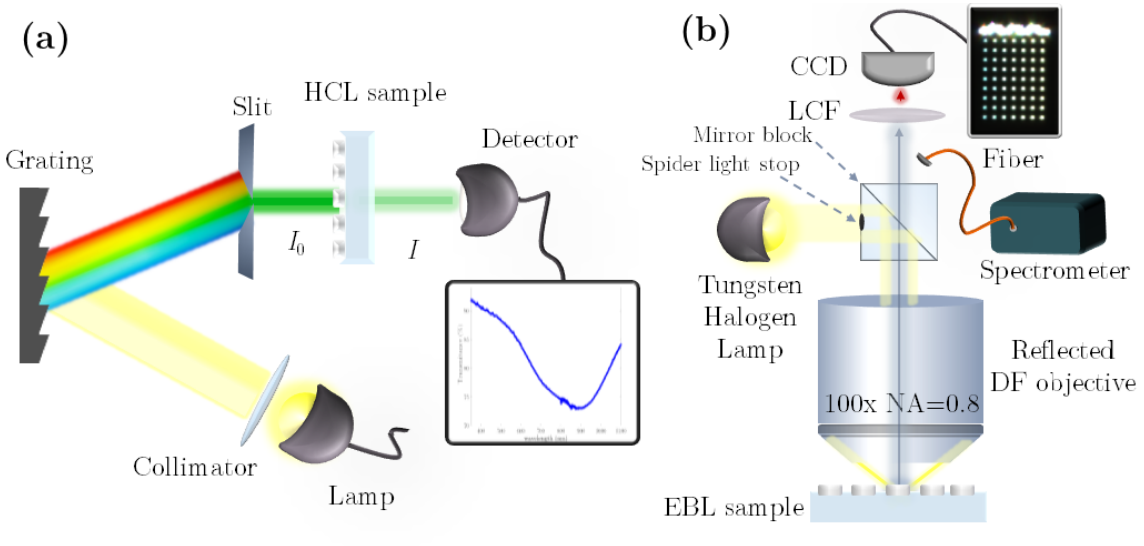

Figure 4.5: *Optical characterization of Al nanodisks (a) Working principle of extinction measurements with a spectrophotometer: collimated light is sent to a monochromator (grating and slit) such that the light transmitted through the sample at each wavelength is recorded. (b) Schema of Dark-Field spectroscopy setup: light is sent in large angles through a* $100\times$ *objective, the scattered light is collected by the objective. The detection can be through a liquid crystal filter (LCF) to record the image of the scattered light at a certain wavelength with a CCD, or through a fiber coupled to a spectrometer.*

nm. One type of spacer consisted on a layer of PolyMethylMethacrylate (PMMA) spin coated and baked at 180°C for 5 minutes. The PMMA was spin coated to vary between 175 and 300 nm in steps of approximately 25 nm.

Another badge of samples were fully fabricated by sputtering. With a top mirror of $t = 5$ nm and a bottom mirror of 100 nm. The SiO_2 thicknesses were $d = 150, 175, 200$ and 225 nm.

4.3 Optical Characterization

Both nanodisks and microcavities were optically characterized. For the nanodisks, the extinction and scattering spectra of ensemble (fabricated by HCL), and single particles (fabricated by EBL), was measured. The ensemble measurements were taken by using spectrophotometer and the single particles were measured by Dark-field spectroscopy in an upright microscope.

In the case of the asymmetric microcavities, their reflectivity spectra was measured at normal incidence in an upright microscope and also the reflectivity in the back focal plane to obtain the dispersion in the cavities. In the following sections the experimental setup is explained.

4.3.1 Ensemble measurements: UV-Vis spectrophotometry

The extinction spectra of the Al nanodisks fabricated by HCL was measured with a UV-Vis-NIR Spectrophotometer (Agilent Cary 5000). The working principle of the spectrophotometer is depicted in figure 4.5. The light from a lamp is collimated and sent to a grating and a slit to obtain monochromatic light. Then, the monochromatic light normally incides in the sample with an initial intensity (I_0), and the intensity of the transmitted light (I) is recorded for each wavelength.

The measurements were done in single beam and transmission mode (% T), such that $T = 100(I/I_0)$. A bare glass substrate was used as baseline. Then, the extinction spectra was calculated from the transmission measurements. The extinction is the sum of the absorption and scattering of the sample. Therefore, assuming that the losses by reflection are negligible, the extinction and transmission spectra are related through $E = -\log(T/100)$.

All the measurements with the spectrophotometer are macroscopic. To measure single particles it is necessary to use a microscope as is explained in the following section.

4.3.2 Single particle measurements: Dark-Field microscopy

Dark-field (DF) microscopy allows us to make sure that the detected photons have interacted with the sample. It is a very useful technique to enhance contrast, thus it is particularly interesting for plasmonic nanoparticles, since they are excellent scatterers.

The general idea of DF is that the light that interacts with the sample is incident in high oblique angles, such that the reflected or transmitted photons that did not interact with the sample are not collected by the detection objective. On the other hand, the photons that interact with the sample are scattered in random directions, therefore some of them will be scattered close to normal incidence, hence will be able to reach the objective.

An important part of DF measurements is how to get the incident light to be only in high oblique angles. For that, in front of the incident beam there is usually a stop, added to a condenser, which blocks the light in the center of the beam. Then the condenser focuses the light cone in the sample.

To measure the scattering spectra of single Al nanodisks an upright microscope was used in DF mode with two kinds of detection: hyper spectral imaging and a fiber coupled to a spectrometer. The schema of the setup is depicted in figure 4.5(b).

First, light from a tungsten halogen lamp is sent to a reflected light mirror block, which has a spider light stop facing the incident light beam. Thus, it blocks the central light beam and reflects the remaining light cone down to a reflective DF objective (Nikon, 100x NA=0.8). This kind of objectives have an inner part that works as a normal objective for the light scattered by the sample (in gray in fig. 4.5(b)) and an outer part that works as a condenser for the incident beam (in yellow in fig. 4.5(b)). Hence, the objective focuses the light cone in the single nanoparticles and gathers the light scattered.

The light collected by the objective was detected by two different means (in separate experiments). In both techniques the reference of the measurements (lamp

spectra) was taken from silica beads randomly distributed. The methods of detections are:

- **Hyperspectral imaging technique**:

  Once the scattered light of the full sample is collected by the objective, it is sent to a tunable liquid crystal filter (LCF) working in the range of 650-1100 nm. Images of the full sample are taken with a EM-CCD camera (Andor iXon) at each wavelength.

  Thus, we obtain an image of the array of particles for each recorded wavelength. Each particle will show a different contrast in the image depending on the scattering intensity of the particle at that specific wavelength. This allows us to reconstruct the spectra of each particle by extracting the intensity values of a given particle in every image [29].

  This is a powerful technique because it allows to measure the scattering spectra of several isolated particles at the same time by obtaining the spectral information from images.

  Figure 4.4(e) shows a stack of the CCD images for all the wavelengths of the LCF. The color is given by the maximum wavelength in the scattering spectra of the particle. Since the measured range is in the red and NIR, the wavelengths in the image are artificially shifted such that the observed color is in the visible region: $\lambda_{imag} = \lambda_{measured} - 220$ nm. We observe that the smallest particles (in the leftmost with d=170 nm) scatter more in the blue and that largest ones (in the rightmost with d=230 nm) scatter more in the yellow part of the spectra. Which is the expected red shift for larger particles.

- **Optical fiber coupled to a spectrometer**:

  In this case, instead of sending the scattered light of the full sample to a CCD, an optical fiber (105 µm) collects the light scattered by a single particle and the spectra of the scattered light is measured with a fiber-coupled spectrometer (Andor Shamrock SR-303i) equiped with a CCD detector (Andor iDus 420).

4.3.3 Reflection measurements of microcavities

For the asymmetric microcavities, the bottom mirror is thick enough so that the light is not transmitted. Then, in an upright microscope we measured reflection at normal incidence. The experimental setup is shown in figure 4.6.

First, the light of a halogen tungsten lamp is focused through a 20x objective (Nikon, NA=0.45) in the surface of the sample. For this measurements the NA of the objective is desired to be low, such that only light reflected at almost normal incidence is collected.

Then the reflected light is collected by the objective and detected by a fiber-coupled spectrometer (Andor Shamrock SR-303). An Ag mirror was used as reference of the reflection spectra of the lamp.

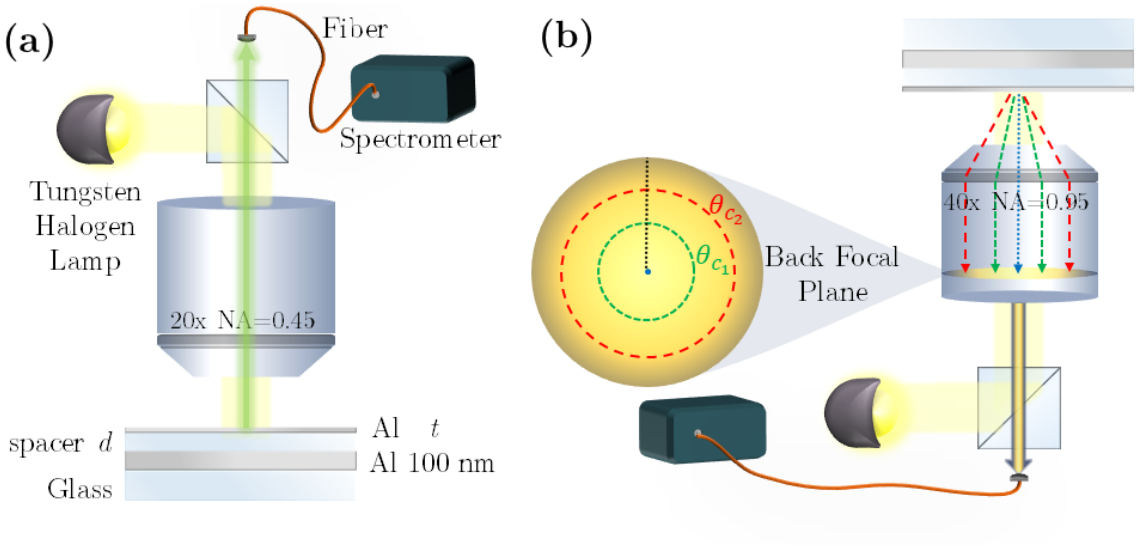

Figure 4.6: *Schema of the reflection measurements setup of the microcavities. (a) Normal incidence. Light is sent and collected at normal incidence and detected by fiber-coupled spectrometer. (b) Dispersion measurements. The microscope is used in back focal plane (BFP) detection, with a very high NA objective (40×, NA= 0.95). Spectra was taken for 4 different points along the black dotted line in the BFP.*

4.3.4 Dispersion measurements

Since the cavities show dispersion, measurements of reflection depending on the angle of incidence were conducted by using a back focal plane (BFP) imaging setup in an inverted microscope (Nikon eclipse TE 2000-E) (fig. 4.6(b)).

All the rays reflected from the sample with the same angles are focused in a circumference of the BFP of the objective, as shown in (fig. 4.6(b)). In the example depicted, all the light reflected with angles θ_{C_2} and θ_{C_1} will be focused and projected as points along the red or green circumferences, respectively. Light reflected in the normal direction is focused in the center of the BFP (blue dot).

Using this setup, light is sent to the sample through a high NA 40x objective (Nikon, NA=0.95), such that some of the light has large incidence angles (up to $\theta = \arcsin 0.95 \approx 72°$). The reflected light at different angles is studied in the BFP, as explained above. For that reason, spectra measurements were done for 4 different points ($\Delta \sin\theta = 0.19$) along the black dotted line shown in figure 4.6(b). The spectra was collected using a 105 µm optical fiber coupled to the spectrometer.

5

Results

The main results obtained are discussed in this chapter, as well as some ideas to follow up the project. The first part focuses on the LSPR-IBT interactions in Al nanodisks. Whereas the second part is devoted to the interactions in the asymmetric microcavities. In both cases the explanation for the calculations is given first, followed by the analysis of the experimental results. Every section has a summary in the last paragraph in order to guide the reader through the results.

5.1 LSPR coupled to interband transitions

5.1.1 Extinction calculations

In order to observe light-matter coupling in Al nanodisks, it is necessary to tune the LSPR response of the disks to be near the frequency of the IBTs. Because, as mentioned in section 3.1, one of the characteristics of strongly coupled systems is the formation of two new eigenmodes when the detuning between the cavity and the emitter is close to zero, $\delta = \omega_c - \omega_0 \approx 0$.

As was pointed out previously, the system considered here is peculiar because the cavity is coupled to an intrinsic property of the material of which it is formed (Al IBTs). Therefore, it is not possible to obtain measurements of the *uncoupled* cavity ω_c, specially at $\delta = 0$. Thus, to know the uncoupled value of ω_c for a specific nanodisk, the extinction spectra was calculated with a dielectric function only with the Drude part, $G_0 = 0$ in equation 2.5.

To be at zero detuning, it is necessary to match the resonance frequency of the nanodisks, ω_c with ω_0, by changing either the diameter, height, or the refractive index of the surrounding media. In figure 5.1, the diameter of a nanodisk is increased from 80 to 200 nm, such that the LSPR is tuned to the IBTs. The IBTs are considered to be centered around the dashed line in figure 5.1, $\hbar\omega_0 \sim 1.5$ eV and to have $\hbar\gamma_0 \sim 500$ meV.

Even when considering the LSPR frequency far from IBTs, there is a clear difference between the spectra when considering IBTs in the calculation (red line in fig. 5.1(b)).

Moreover, two peaks with similar intensity appear at $\delta = 0$ when considering the IBTs contribution. On the contrary, there is only one peak without the IBTs (fig. 5.1(b)). Meaning that the system is coupled.

For instance, it is possible to smoothly tune ω_c towards ω_0 by changing the refractive index that surrounds the disk. The variation of the uncoupled cavity is

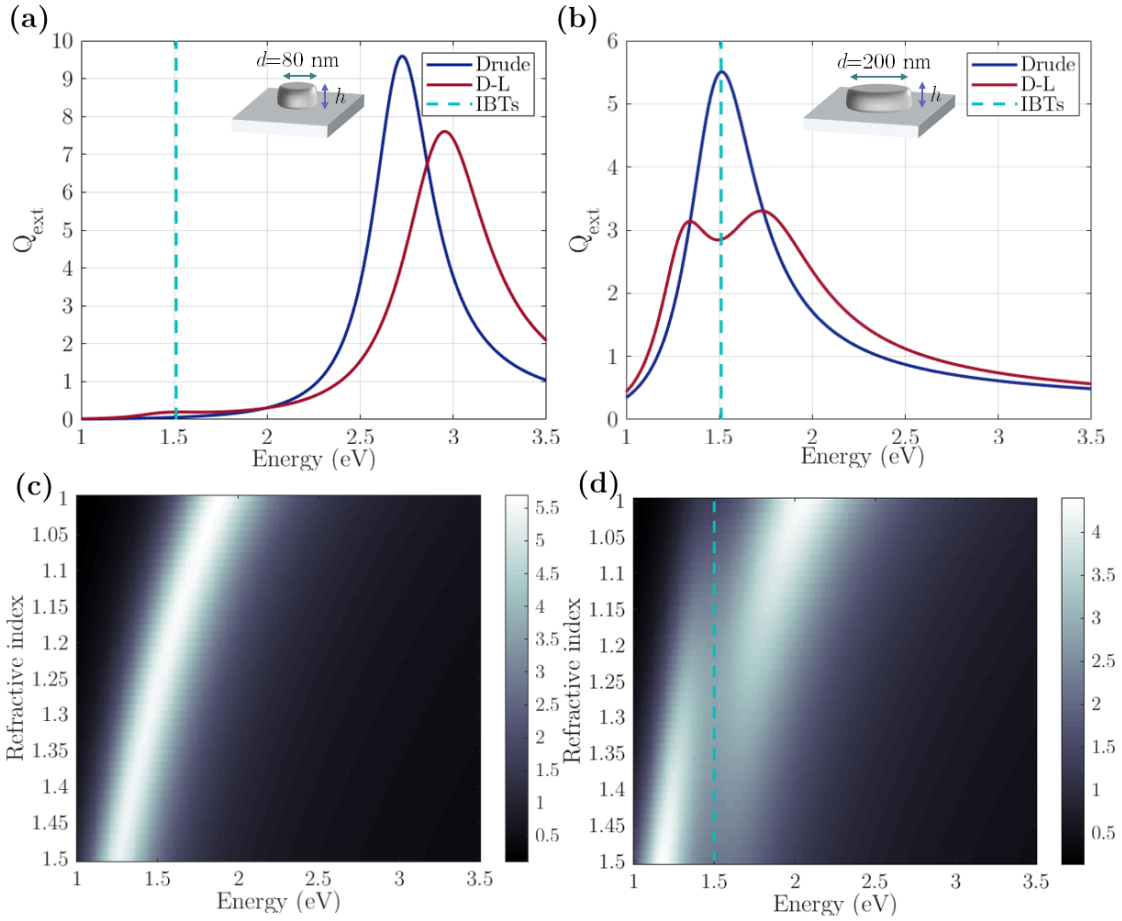

Figure 5.1: *Calculated extinction efficiency (Q_{ext}) of Al nanodisks. The disks are 10 nm in height and a diameter of (a) 80 nm, such that LSPR is far from Al IBTs, and (b) 200 nm to obtain an overlap of LSPR and IBTs. (c) Uncoupled cavity mode of a nanodisk with d=200 nm and h=10 nm when changing the refractive index of the surroundings. (d) Anticrossing of the cavity mode (on the left) and the IBTs (in blue).*

shown in figure 5.1(c) and an anticrossing behaviour between the cavity and the IBTs is observed when using the full Drude-Lorentz model (figure 5.1(b)). In fact, figure 5.1(b) is a cross section at $n = 1.25$ of figure 5.1(c) and (d).

The anticrossing is a clear indication of the interaction between the IBTs and the LSPR. Nonetheless, to determine whether it can be considered a strongly coupled system (eq. 3.3), it is necessary to calculate the coupling strength, g.

To obtain the coupling strength of the LSPR-IBTs, the extinction spectra of the nanodisk was calculated using the coupled oscillator model, COM (sec. 3.2). The two oscillators are given by the IBTs and the LSPR response (as the cavity). IBTs were considered with $\hbar\omega_0 = 1.5$ eV and a linewidth of $\hbar\gamma_0 = 500$ meV. The frequency of the cavity and its linewidth, ω_c and γ_c, vary depending on the geometry of the nanodisk.

Let us follow up the example given in figure 5.1(b), where $\hbar\omega_0 \approx \hbar\omega_c \approx 1.5$ eV (fig. 5.2(a)). The linewidth of the uncoupled cavity, γ_c, is calculated from the

Drude response (dark blue spectra). Then, the obtained values of ω_c and γ_c are used to fit the DL spectra (red line) with the COM spectra (light violet line).

The anticrossing plots (fig. 5.2) show that $\delta = 0$ for a nanodisk with $h \sim 9.8$ nm, $d \sim 203$ nm and $n \sim 1.25$. That geometry is very close to the one considered in fig. 5.2(a). In that case for COM, it is considered that $\hbar\omega_c \sim \hbar\omega_0 = 1.5$ eV, $\hbar\gamma_0 = 500$ meV and $\gamma_c = 435$ meV. The COM coupling strength is then $\hbar g = 460$ meV. Let us note that, g given by COM was similar to the energy splitting for all the calculations. This could happen since for the COM the coupling strength does not necessarily has the same physical meaning as in the Hamiltonian (eq. 3.1).

In this case, $\hbar(\gamma_0+\gamma_c)/2 = 467.5$ meV, and the Rabi splitting by COM is ~ 460 meV. Then, the LSPR-IBT system is on the edge of strong coupling. By considering the energy difference between the two peaks at zero detuning in the plots in figure 5.2, $\Omega_R \sim 390$ meV. Thus, COM gives a slightly larger value of the splitting at zero detuning.

Also, in this specific case g varies for different δ, because δ depends on the geometry of the disks, then $g \propto \mu\sqrt{1/V}$. Where μ is the dipole moment of the emitter (IBTs) and V the mode volume of the cavity. The mode volume will be different for different geometries of the cavities. As discussed previously, the mode volume in plasmonic nanoresonators is not trivial [20]. Nevertheless, here a direct variation of the mode volume (V) with the geometrical volume ($\mathcal{V}$) was assumed. This approximation is valid considering that in metallic nanoparticles the mode is concentrated within it [4]. However, it is necessary to be careful, since the mode volume for lossy cavities is not easy to define [30].

Let us consider the case of refractive index variation with fixed geometry (h=10 nm, d=200 nm). Fig. 5.2(b) shows color maps of the extinction spectra for the former disks. The uncoupled modes are marked with dashed lines and the maxima of Q_{ext} are shown in red crosses. The maxima given by COM are marked in circles, for that fit g decreases from 500 meV to 410 meV when increasing n from 1 to 1.5. This makes sense, because the mode will leak more into the surroundings when increasing n.

Varying the refractive index of the surrounding media has the advantage of maintaining the geometry of the cavity, decreasing any extra variation given by the shape. But it is not simple to tune the refractive index experimentally. It is more viable to tune the frequency of the cavity by changing either the height (h) or the diameter (d) of the disks. The anticrossing in the case of those variations is shown in figures 5.2(c) and (d).

Considering the diameter of the nanodisks as a variable to tune ω_c, and by assuming that mode volume varies directly as the volume of the disk, the increase of g has to be linear because $\mathcal{V} \propto d^2$ and $g \propto 1/\sqrt{V} \propto 1/d$. Thus, a linear variation of g for the COM (inset in fig. 5.2(c)), is assumed such that it decreases from 510 to 400 meV when d increases from 170 to 230 nm.

In analogy, $\mathcal{V} \propto h$. Therefore, $g \propto 1/\sqrt{h}$ can be expected. The COM fit for such dependence is shown in figure 5.2(d). As shown in the inset, the variation of g is an almost linear decrease from 460 to 300 meV when increasing the height from 10 to 30 nm.

Calculations were made under several approximations, such that the disks are

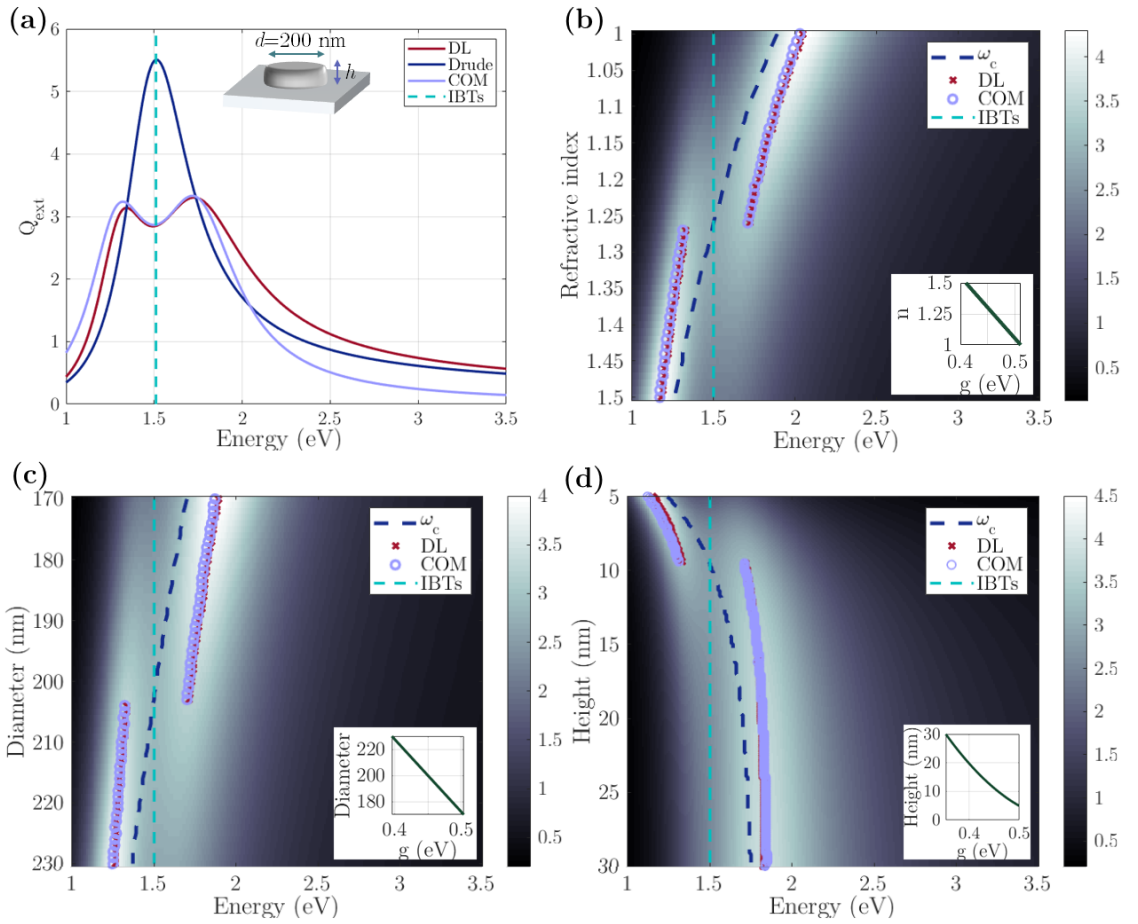

Figure 5.2: *Coupled Oscillator Model fitting to Q_{ext} spectra calculated using DL model. (a) Example of the fitted spectra for a disk of d=200 nm, h=10 nm and $n = 1.25$. Anticrossing between IBTs and LSPR with the maximum of the DL and COM spectra highlighted. The anticrossing is obtained by varying: (b) n of a disk of d=200 nm and h=10 nm, (c) diameter of a disk of h=10 nm with $n = 1.25$ and (d) height of a disk of d=200 nm and $n = 1.25$. The variation in g is shown as an inset in each plot.*

ellipsoids and that they are surrounded by homogeneous media. Even though, the disks are sitting on glass, covered by a self-limiting layer of Al_3O_2 of around ~ 3 nm [11] and surrounded by air. Also, let us be aware that the size of the disks used here is already not strictly considered by MLWA. Thus, we should be careful with claiming anything without the experimental results.

In brief, mode splitting was observed in calculations of LSPR−IBTs interactions via extinction spectra. By using COM, a decrease in g is observed when increasing the volume of the particle and when increasing n, which is attributed to the increase of the mode volume of the cavity. The value of g is always around $\sim 350 - 500$ meV. Furthermore, at $\delta = 0$, $g \approx 460$ meV. By relating this value to the energy splitting, we can say that the system is on the edge of strong-coupling. Nevertheless, we should be cautious, because the observed splitting at $\delta = 0$ in figure 5.2 is 390 meV, which is not enough for the system to be in strong coupling.

5.1.2 Ensemble experiments

To measure LSPR-IBT interaction, the height of HCL Al nanodisks was varied while keeping the diameter fixed to 172 nm and 200 nm. Once the 172 nm nanodisks were optically characterized, a layer of PMMA was deposited on top to redshift their extinction spectra by increasing the refractive index of the surrounding media.

The extinction spectra measured for all the samples is shown in figure 5.3(a-c). The first and second column contain the measurements for nanodisks with 172 nm of diameter, but for the second column the disks are covered with PMMA. For the third column, $d = 200$ nm. As expected, the LSPR blueshifts when increasing height and redshifts when the diameter and refractive index increase.

Even though it is possible to observe damping and broadening of the LSPR around $\hbar\omega \approx 1.5$ eV, there is not a clear mode splitting as calculations indicated. This is related to the dielectric function of Al.

The dielectric function used in calculations, $\varepsilon(\omega)_{DL}$, was fitted to the experimental data by Racik et al. [2]. Nonetheless, ε strongly depends on Al deposition conditions [11]. If the deposition rate is slow and the vacuum is not good enough ($> 10^{-7}$ Torr), the amount of oxide inside the nanodisk increases (apart from the ~ 3 nm formed on the surface). This decrease in Al quality damps the magnitude of both the imaginary and real part of ε [11].

In order to take this damping into account to fit the experimental data, the oscillator strength of IBTs, G_0, was decreased in the calculation of ε_{DL} from 13 to 5.2 (fig. 5.3(d-f)). This is an approximation, in reality most of the parameters in equation 2.5 should slightly change to fit the experimental ε, in particular ω_P.

The best way to do the calculations would have been to measure ε of the deposited Al by ellipsometry and then fit again ε_{Al} with DL model to the measured data, or even use the measured data for the calculations directly. Another possibility is to measure the amount of Al_2O_3 in bulk Al by X-ray Photoelectron Spectrosocopy (XPS) and use Bruggeman model to calculate the dielectric function as made by Knight et al. [11].

However, the mentioned rough approximation was enough to fit the measured data and calculate ω_c and γ_c for the three batches of samples (fig. 5.3(d-f)). With the Drude part information, the linewidth and resonance of the uncoupled cavity was estimated and the COM was used to fit the experimental data to obtain g.

As mentioned previously, g depends on the size and the surrounding media of the nanodisks. The COM fit and the value of g for each curve is shown in figure 5.3(g-f). In this case, $g < 300$ meV, which is ~ 150 meV ($\sim 33\%$) smaller than the calculated one. Thus, the system would is now on the weak coupling regime.

Moreover, if we consider the anticrossing plots for calculations considering the low quality Al with $G_0 = 5.2$ (fig. 5.4), mode splitting is barely visible in both cases and the uncoupled IBTs moved from 1.5 to 1.55 eV. Plots in figure 5.4 also show that the experimental system is in the weak coupling regime.

In a more rigorous perspective, the splitting should be measurable in absorption to make sure the system is strongly coupled. To measure it, an integrating sphere in Cary 5000 would be required [10]. However, no mode splitting was observed in absorption calculations even for good quality Al. The problem with absorption is that it is weak in comparison with scattering, because the nanodisks are

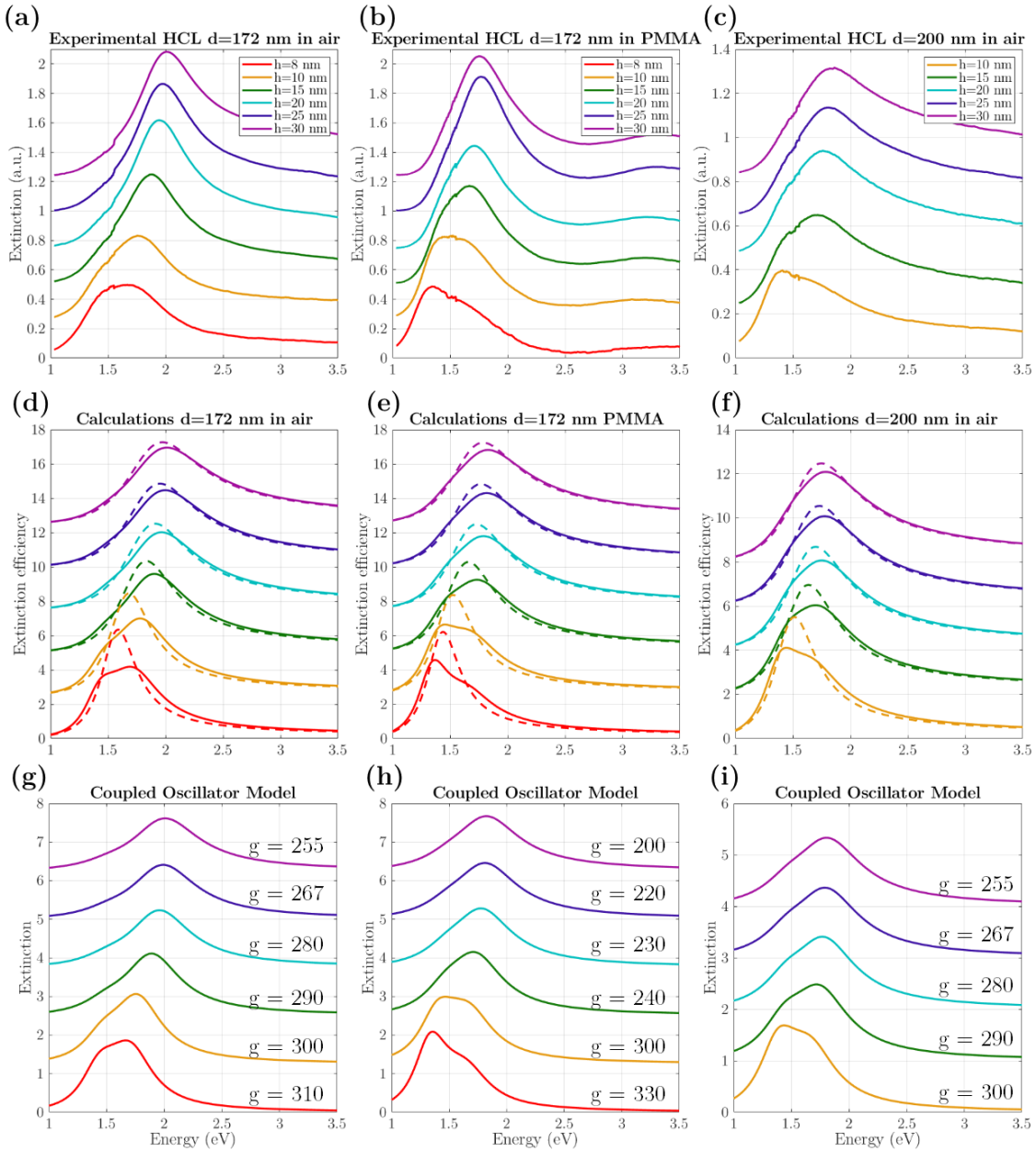

Figure 5.3: *(a-c) Extinction measurements of Al nanodisks fabricated by HCL. The extinction for different heights is shown with an offset in each plot. (d-f) Extinction calculations using MLWA to fit the experimental data. Made considering a low quality Al ($G_0 = 5.2$). The Drude spectra is shown in dotted lines. (g-i) Extinction calculations using the Coupled Oscillator Model for a given coupling strength. The first column from left to right shows the results for nanodisks of d=172 nm, the second column shows results of the same nanodisks covered in PMMA and the third column has d=200 nm.*

quite large. Therefore, to enhance the absorption we could decrease the size of the particles, which is hard because it is necessary to tune the LSPR to NIR part of the spectra. Making small disks to enhance absorption was simpler for Pirzadeh et al., since Ni IBTs are in the UV [10].

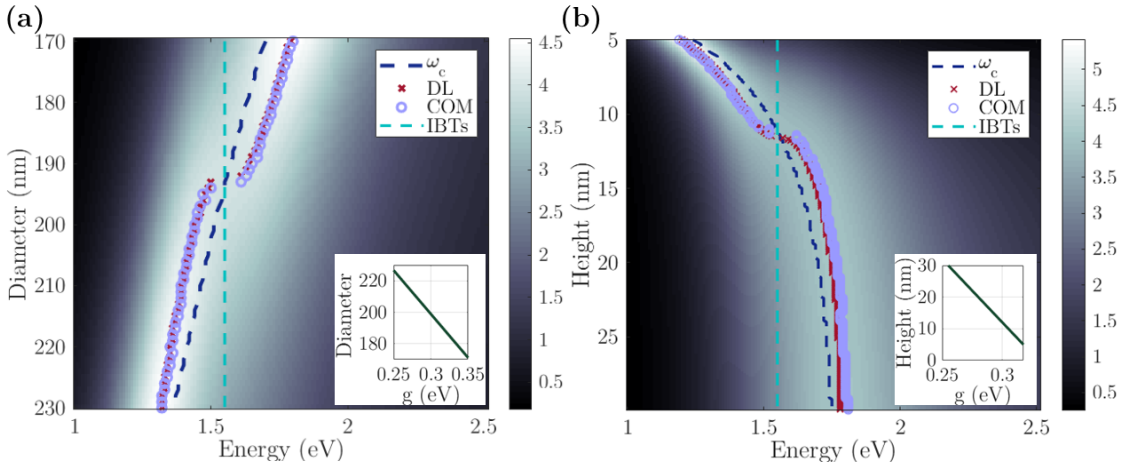

Figure 5.4: *Coupled Oscillator Model (COM) fit of Q_{ext} spectra calculated using DL model with $G_0 = 5.2$. (a) Variation in diameter with $h = 10$ nm and $n = 1.25$. (b) Variation in height for a disk of $d = 200$ nm and $n = 1.25$. The insets show the values of g for the COM.*

In short, due to the quality of the Al, the experimental coupling strength is $\sim 33\%$ weaker than expected through calculations. Thus, to increase IBT-LSPR interaction it is important to be careful with Al deposition conditions. For that it is better to deposit Al under very good vacuum ($< 10^{-7}$ Torr) at a constant 20 Å/s rate.

5.1.3 Single particle experiments

Fabrication of single particles was planned in order to decrease the linewidth of the LSPR by removing the broadening given by size dispersion of nanodisks fabricated by HCL. In addition, measurements of the scattered light are directly comparable with calculations. Because strictly speaking, UV-Vis spectrophotometry does not measure directly the extinction of the sample. It measures transmission, from which we can calculate the extinction by assuming that losses by reflection are negligible.

For this, two batches of Al nanodisks were fabricated to compare the deposition rate influence on the scattering spectra, as was discussed above. One of the depositions had an increasing rate from 1-2 Å/s and the other was fixed at 20 Å/s. The height of the disks was fixed to 20 nm and the diameter varied every 10 nm from 170 to 230 nm. Also, PMMA was deposited on top later to redshift the spectra.

As mentioned in chapter 4, two different detection methods were used: hyperspectral imaging technique, and a fiber coupled to a spectrometer. The results of both techniques are shown in figure 5.5. It also shows calculations on the expected scattering cross section spectra for a low quality Al ($G_0 = 5.2$).

Unfortunately, there are discrepancies between the two measurements and the calculations. SEM images were taken before the measurements and the geometry of the particle was as expected (fig. 4.4(d)). Therefore, such discrepancies may be related to oxidation of bulk Al.

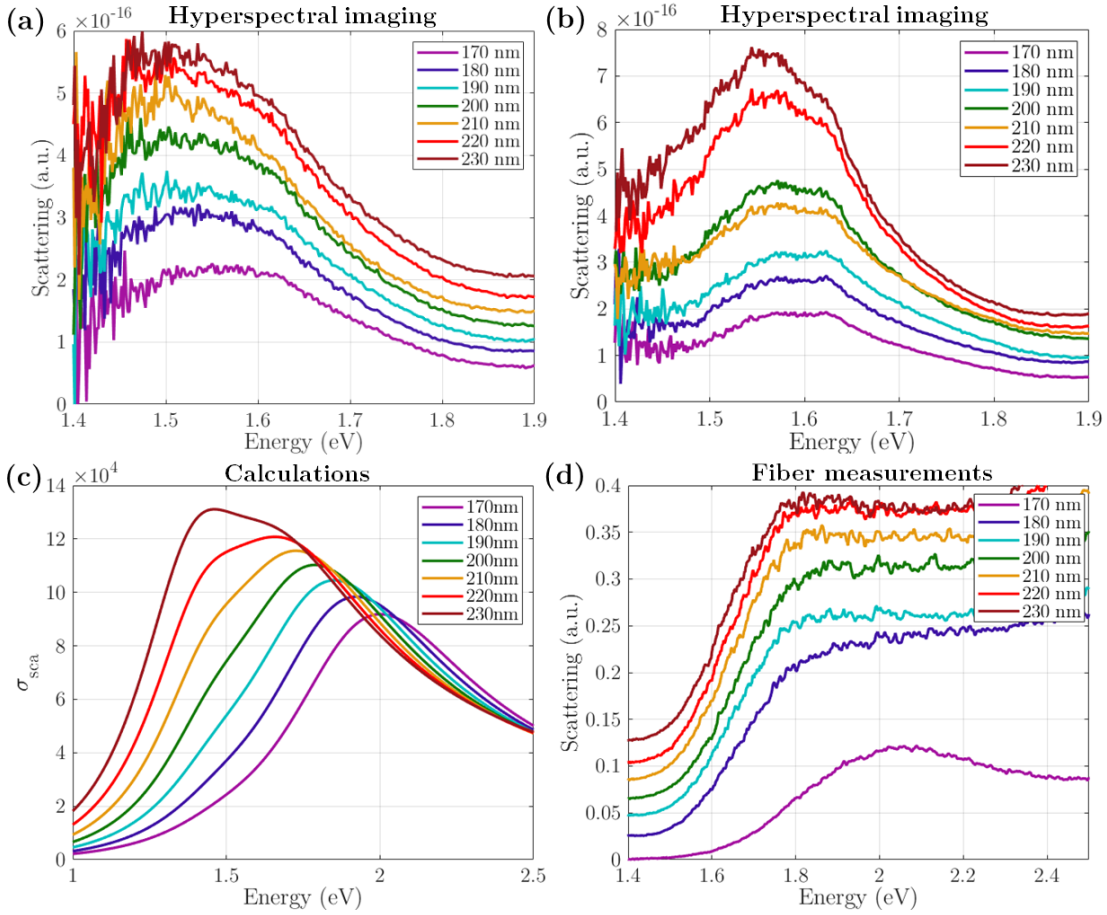

Figure 5.5: *Hyperspectral imaging technique measurements for Al deposited at (a) 1-2 Å/s and (b) 20 Å/s. (c) Calculations of the scattering cross section considering a low quality Al ($G_0 = 5.2$). (d) Spectra of nanodisks deposited at 20 Å/s done by fiber coupled to a spectrometer. Note that the scale of the axis is different for each plot.*

However, measurements via two detection techniques should show similar results even if Al was oxidized. Meaning that there was a particular issue with the measurement setup. Hyperspectral imaging was also utilized on Au bipyramids with a known scattering spectra to make sure the setup was not the problem. Nevertheless, Au bipyramids scattering efficiency is much better than Al nanodisks. Hence, the problem may be the low scattering efficiency of single Al nanodisks, along with the low halogen lamp intensity at the wavelengths of interest. Which is too low for energies below ~ 1.4 eV. Giving a low light intensity to measure.

Also, the spectra for energies larger than ~ 1.65 eV decays similarly for all the particles, which seems more of an artifact than a real signal. This leaves a very short energy range that is measurable. Within this range, it is possible to compare the scattering spectra for a diameter of 220 and 230 nm, and find a similar behaviour. But the range is too short to conclude anything beyond a reasonable doubt.

Measurements with the fiber coupled spectrometer showed the same problem with intensity at low energies. Such that, the decay in the signal below ~ 1.8 eV

resembles more of an artifact. An extra issue with this technique was that the spectra are enhanced for larger energies, hindering the signal at the region of interest. There is no clear explanation for this, since the measurements consider the background and they are normalized to the lamp signal.

The samples were covered with a layer of PMMA to redshift the scattering peak, but the measurements were taken with a fiber coupled to a spectrometer and are very similar to the ones in fig. 5.5(d).

Even though it was not possible to measure single particles, Halas group has measured single Al nanodisks with around the same geometry and observed a dip in the scattering spectra that they also attribute to the IBTs [31].

In summary, measurements of single particles were not reliable. Therefore, it is not possible to make statements regarding the IBT-LSPR interaction in this case.

On the whole, by using simple plasmonic nanoresonators, weak LSPR-IBT interaction was measured in Al by observing slight mode splitting in the extinction spectra. Even though, strong coupling was not observed it was possible to enhance the absorption rate of IBTs in Al, by simply reshaping Al into nanodisks of the right dimensions. Moreover, calculations show that it is possible to be on the edge of strong coupling in this systems if the quality of Al increases.

5.2 Asymmetric microcavities

Plasmonic nanoresonators are interesting for IBT-light interactions, because they are *simple* to fabricate and have very small mode volume. A simpler structure to fabricate in which we can study light-IBT interaction is a microcavity, which can even be fully fabricated in the same deposition system without breaking vacuum.

As mentioned before, asymmetric microcavities can be designed to be perfect absorbers at a given wavelength. Such that most of the absorbed power is localized in the top mirror. Also, when decreasing the thickness of the top mirror, the quality factor decreases. Thus, part of the field *leaks* into the upper mirror, enhancing light-IBT interactions.

Therefore, TMM was used to calculate the absorption of asymmetric microcavities with the structure showed in figure 2.2(c). Similar to the calculations for nanodisks, ε_{Al} was given by Drude-Lorentz model.

Figure 5.6 shows the calculated reflectivity spectra at normal incidence. The left column shows the spectra for a stack with the different layers for a given spacer thickness. The IBTs of the bare Al bottom mirror cause a dip in reflection around ~ 826 nm (~ 1.5 eV) as shown in (a). Then, the spacer (200 nm thick with $n = 1.45$) gives rise to another dip in the UV due to a second order mode in a Salisbury screen formed by the reflected and transmitted light by the spacer-air interface (b). By calculating the reflectivity using only ε_{Drude} we observe two dips in reflection due to the formation of the microcavity (c). If we consider also IBTs in Al, the uncoupled cavity modes show a slight *repulsion* between the dips given by the cavity and by IBT, giving rise to a weak mode splitting (d). Also the absorption by the IBTs is enhanced when the cavity mode is close, which is expected from Purcell effect.

The uncoupled optical mode redshifts when increasing the distance light travels inside the spacer. The distance can be varied by changing the angle of incidence of

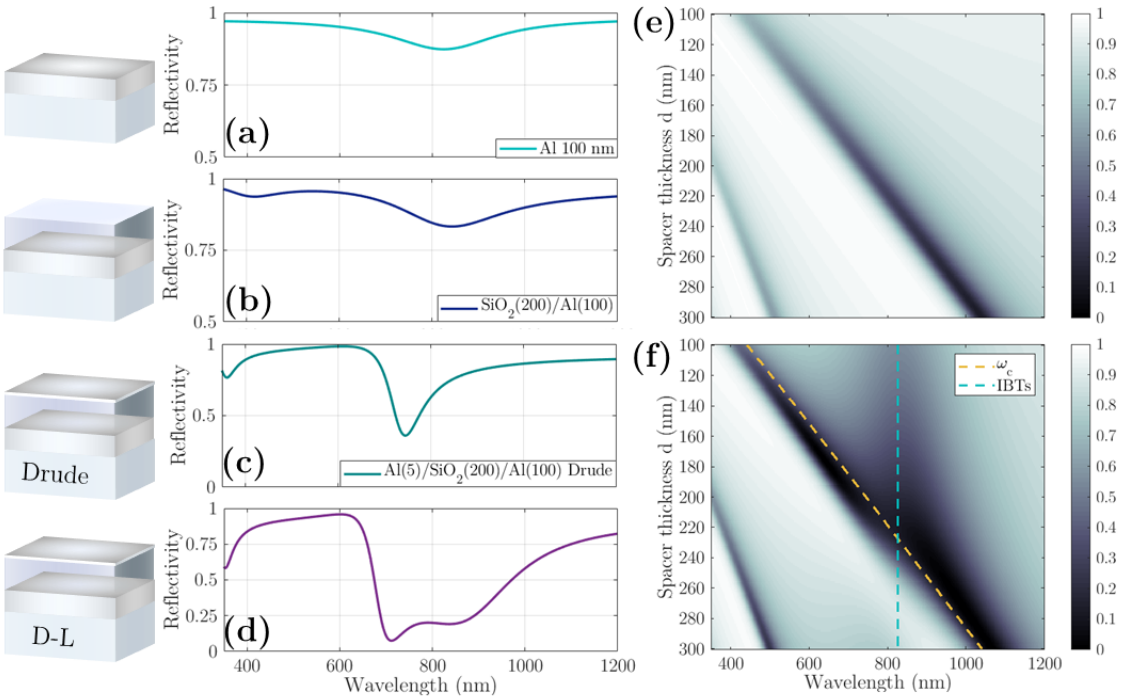

Figure 5.6: *Reflectivity calculations of the asymmetric cavities by TMM. (a) R for a 100 nm thick Al bottom mirror. (b) R of the mirror with a 200 nm thick layer of SiO_2 on top, $n = 1.45$. (c) R for a cavity with $t = 5$ nm for the top mirror, considering ε_{Drude}. (d) Cavity with $t = 5$ nm and the full DL model, with $G_0 = 13$. (e) Uncoupled cavity mode depending on the spacer thickness, d ($G_0 = 0$). (f) R dependence on d with IBTs ($G_0 = 13$). The uncoupled components are shown in dashed lines.*

light (dispersion) or the spacer thickness, d, at normal incidence. Thus, the detuning between the cavity mode and the IBTs was varied to achieve $\delta = 0$ by changing the spacer thickness.

The uncoupled mode of the cavity, considering only the Drude part of Al, dependence on d is shown in figure 5.6(e). Note that the color map goes from 0 to 1 in reflectivity. As expected, the wavelength of resonance of the cavity increases linearly with the thickness of the spacer between both mirrors and a second order mode appears for thicker cavities.

When including the IBTs in calculations a weak interaction is observed, since near $\delta = 0$ the cavity mode slightly blue-shifts (fig. 5.6(f)). But the two modes are not clearly observed at zero detuning ($d = 218$ nm).

First, the impact of the top mirror thickness, t, on IBT-cavity mode interaction was studied. When increasing t, the coupling becomes less clear. This is attributed to two reasons. The first one is the difference in linewidths of IBTs and cavity mode. Since for $t = 5$ nm, $\gamma_c \sim 430$ meV, which is comparable to the dissipation in IBTs (~ 500 meV). Whereas for $t = 15$ nm, $\gamma_c \sim 43$ meV. In which case, for the mode splitting to be real (eq. 3.3) g would have to be larger than ~ 450 meV.

Secondly, the Q factor increases rapidly with the thickness of the top mirror. Such that, $Q \sim 9$ for a top mirror of $t = 5$ nm, and $Q \sim 43$ when $t = 15$ nm. Thus,

the absorbed power in the top mirror decreases, because most of the incident light will be reflected by it before entering the cavity. Consequently, a thinner mirror is preferred. For the rest of the calculations only 5 nm thick top mirrors were considered. It is important to keep in mind that thinner mirrors are a challenge to be controlled experimentally.

An interesting feature that is observed in figure 5.6(f), that still remains unexplained, is that the dip in reflection given by the IBTs disappears after the optical mode interacts with it (for $d > 260$ nm).

Additionally, as expected from the nanodisks results, cavity-IBT interaction decreases when the oscillator strength of the IBTs diminishes.

Summarizing, even in this simple structure the calculations showed IBTs-cavity weak interaction. It is weaker than in nanodisks, probably because the mode volume is larger. As before, a stronger interaction is expected for a good quality Al microcavity with a 5 nm thick top mirror.

5.2.1 Measurements of the microcavities

Optical characterization of the microcavities consisted on measuring reflection at normal incidence and dispersion, as explained before (sec. 4.3.3).

The cavities were fabricated with different spacer thicknesses with a 5 nm thick top mirror. TMM calculations for the same thicknesses are shown in figure 5.7(a), whereas the reflection measurement at normal incidence is shown in (b). The calculations considered low quality Al ($G_0 = 5.2$). Discrepancies in the dips in reflection between calculations and experiments may be given due to the quality of the deposited SiO_2, which may have a lower refractive index due to porosity and impurities in sputtering.

The dip given by the optical mode redshifts towards the IBTs when increasing SiO_2 thickness. The interaction between both is clearer for $d = 225$ nm, since the detuning, δ, is reduced. Similar to the LSPR-IBT interaction, the optical mode looses intensity and broadens, while the dip caused by the IBTs is enhanced.

Dispersion measurements allow to obtain different detuning values for the same sample by changing the angle of incidence. This makes anticrossing measurements possible with a single sample [4, 32]. Figure 5.7(c) shows dispersion measurements for a cavity with $d = 225$ nm. When decreasing the angle of incidence, the cavity mode redshifts, and starts merging with the IBTs. Unfortunately the samples were not thick enough to be able to catch the avoided crossing behaviour in one sample via dispersion measurements.

Even though the structure of the cavities is very simple, it is necessary to be careful during fabrication to obtain reproducible samples if a good quality of Al is required. Because, Al quality increases with the rate of deposition, but if only 5 nm of Al are required on top, the deposition lasts for $\sim 2-3$ seconds. Usually there will be a slight error in the thickness of the top mirror related to the deposition system. In addition to that, a self-limiting native oxide layer (Al_3O_2) of around $\sim 2-3$ nm will be formed [11]. The thickness of the oxide layer on top and the real thickness of the top mirror could be measured by XPS.

The fabrication process can be improved to increase reproducibility control.

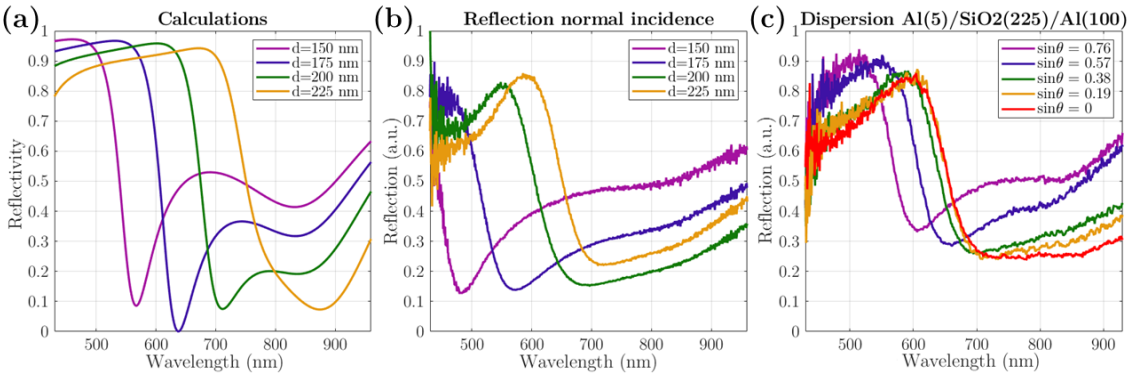

Figure 5.7: *(a) Calculations for different spacer thickness, d, with $t = 5$ nm and $G_0 = 5.2$ (b) Normal incidence reflection measurements of asymmetric microcavities ($Al(5)/SiO_2(d)/Al(100)$) for different d. (c) Dispersion measurements of a microcavity with $d = 225$ nm and $t = 5$ nm.*

Such as, not breaking the vacuum while depositing, and stabilize the evaporation rate to 20 Å/s before opening the shutter, and that it can be closed fast enough once the desired thickness is reached.

Briefly, it was possible to measure weak light-IBTs interactions in asymmetric Al cavities. To be sure about the coupling it would be better to have a sample with an optical mode at normal incidence redshifted from the IBTs in order to observe the anticrossing behaviour in dispersion measurements. For that, also the deposition process should be improved to obtain better quality of Al and better reproducibility.

5.2.2 Molecule on top of the cavity

After noticing the large effect the oscillator strength, G_0, has on the IBT-LSPR coupling strength, and considering the general idea of *coupling strength borrowing* proposed by Bisht et al [32]. The possibility of a system composed of three elements was considered where IBTs, light, and a molecule resonant with the IBTs interact to increase the coupling strength of the full system.

Hence, additional TMM calculations were made considering a layer of molecules on top of the cavity. For that, the refractive index for the layer of molecules was calculated using a Lorentzian dielectric function,

$$\varepsilon_{mol}(\omega) = \varepsilon_\infty + \frac{f\omega_{mol}^2}{\omega_{mol}^2 - \omega^2 - i\gamma_{mol}\omega}. \tag{5.1}$$

The parameters were chosen as realistic values for molecules: $\varepsilon_\infty = 1.45^2$, $f = 1$ and $\hbar\gamma_{mol} = 0.1$ eV, with the same resonance frequency as the IBTs of Al, $\hbar\omega_{mol} = 1.58$ eV.

The left column of figure 5.8, shows the reflection spectra of the different layers of the stack, in analogy to figure 5.6. The reflectivity of the bare 20 nm thick layer of molecules on top of the bottom mirror is shown in (a). When the molecules are separated from the top mirror by a spacer a mode is generated, shown in 5.8(b), similar to fig. 5.6, but such mode does not interact with the absorption dip in

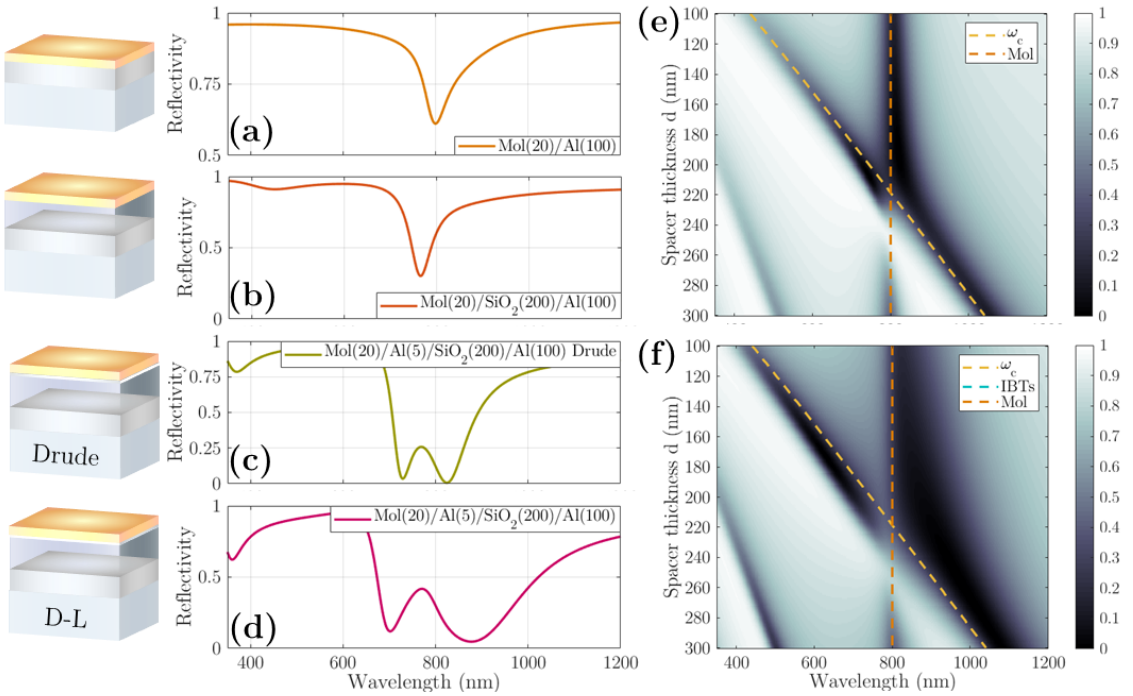

Figure 5.8: *R calculations for cavities with a $h = 20$ nm layer of molecules resonating in $\hbar\omega_{mol} = 1.58$ eV on the top. (a) R for a 100 nm thick Al bottom mirror. (b) R of the mirror with a 200 nm thick layer of SiO_2 on top, $n = 1.45$. (c) R for a cavity with $t = 5$ nm for the top mirror, considering ε_{Drude}. (d) Cavity with $t = 5$ nm and the full DL model, with $G_0 = 13$. (e) Cavity mode depending on the spacer thickness, d ($G_0 = 0$), with molecules on top ($h = 20$ nm). (f) R dependence on d with IBTs ($G_0 = 13$) and a 20 nm layer of molecules on top. The uncoupled components are shown in dashed lines.*

the molecules. When adding a thin top mirror in between the molecules and the spacer, even without considering IBTs, there is mode splitting of $\sim$ 200 meV (fig. 5.8(c)). Meaning that the molecule interacts with the optical mode even without the IBTs. This is because the cavity mode without considering the IBTs has a frequency and FWHM very similar to the molecule (see (b) in figures 5.6 and 5.8), such that $\gamma_c \sim \gamma_{mol}$.

Moreover, when considering also the IBTs, the previous mode splitting increases up to $\sim$ 360 meV. Let us remember that in IBTs-light system (fig. 5.6(d)) the splitting is of $\sim$ 270 meV for the same spacer distance ($d = 200$ nm). Meaning that, both the IBTs-light interaction and the molecule-light interaction are enhanced when considering the 3-component system, in line with Bisht et al. study [32].

Furthermore, the difference in avoided crossing between light-molecule and light-IBTs-molecule is visible in 5.8(e) and (f). The Rabi splitting of the 3-component system is considerably larger, increasing from $\sim$ 155 meV to $\sim$ 285 meV (figure 5.9(c)).

Two important things should be highlighted. The first one is that the molecule layer shows mode splitting even without the IBTs, suggesting that one can use these Al cavities for light-molecule coupling even when the molecule is not in resonance

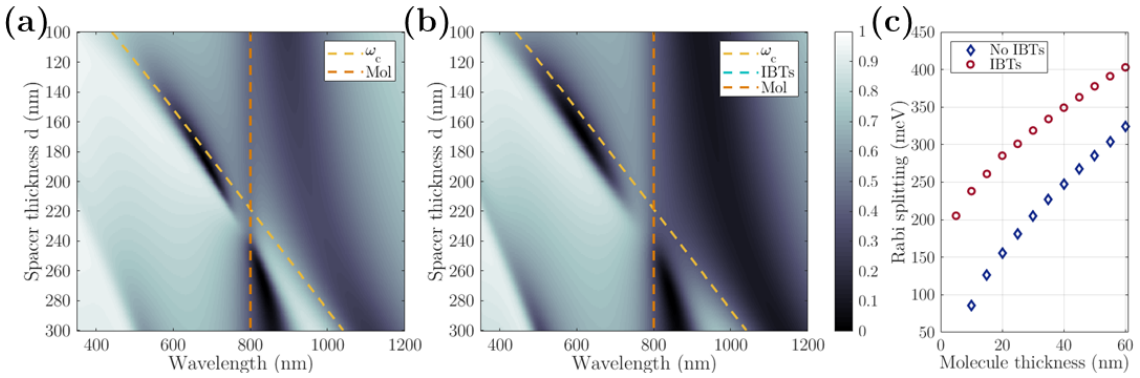

Figure 5.9: *(a) Reflectivity of a 70 nm thick layer of molecules on top of the cavity (b) R for molecules (h = 20 nm) on top of the cavity with IBTs. (c) Variation of the Rabi splitting (δ = 0 m for d = 218 nm) with the thickness of the layer of molecules.*

with the IBTs. The second one is that the interaction of the IBTs-light and light-molecule is enhanced when the 3 systems interact at the same time.

Mode splitting in figures 5.8(e) and (f) increase when the layer of molecules increases up to a thickness of 50 nm, at this point the absorption of the bare molecule appears in the spectra as shown in figures 5.9(a) and (b). The increase in Rabi splitting for the cavity-molecule system and cavity-molecule-IBTs is shown in figure 5.9(c). The problem with thick layers is that the cavity modes formed by the molecules layer on top change the uncoupled cavity mode, so it is not as simple as the yellow dashed line depicted in 5.9(a-b).

This study is similar to the one made by Antosiewicz et al. where the coupling between a Ag nanosphere and a Dye coating was theoretically studied, for different geometrical and dielectric function parameters [33]. The difference is that here an extended cavity is studied and the interaction involves 3 components: molecules, IBTs, and the cavity mode.

Another important aspect to highlight is that in order to claim a strongly coupled system it is crucial to observe anticrossing also in absorption spectra. In this case, given that the transmission of the cavity is basically zero due to the bottom mirror, the anticrossing in absorption is observed, because $A = 1 - R$.

In summary, IBTs-light interaction increases when molecules resonant with the IBTs are located on top of the cavity. A stronger interaction of the 3-component system is observed, since the Rabi splitting of the molecule-cavity system ($\sim$ 155) meV increases to $\sim$ 285 meV when adding the IBTs. Furthermore, for the molecules to show mode splitting with the cavity it is not necessary for them to be resonant with the IBTs. Thus, this system has potential as an open and extended cavity.

5.2.3 WSe_2 on top of the cavity

For a experimental realization of the previous theoretical study, a material with a resonance very close to the IBTs of Al is required. Such material can be WSe_2. This Transition Metal Dichalcogenide (TMD) has its A-exciton around $\hbar\omega_0 \sim 1.61$ eV [34]. Thus, it can be useful for an experimental realization of the previously explained 3-component system in the proposed extended cavity.

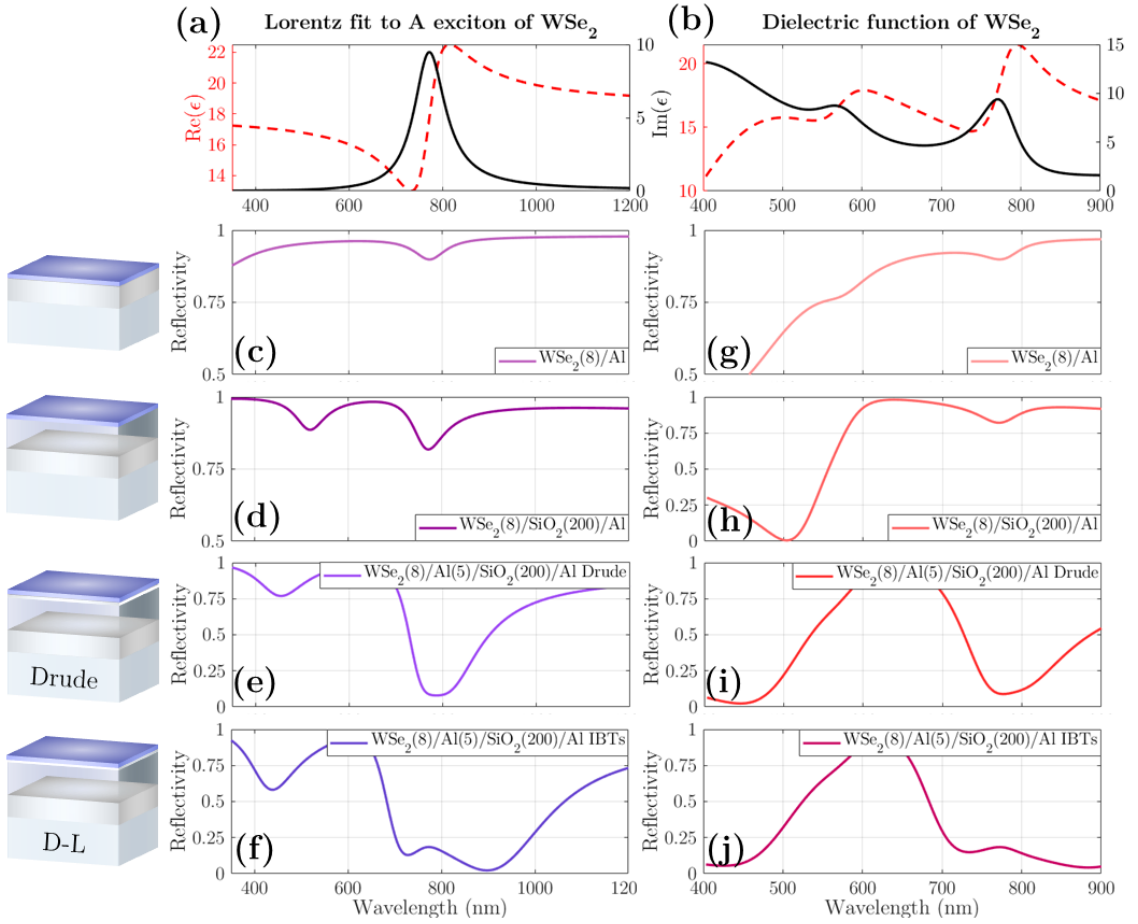

Figure 5.10: *Reflectivity calculations for different stacks considering WSe_2 on top of the cavity. The spacer thickness is $d = 200$ nm and the WSe_2 thickness is $h = 8$ nm. Left column: calculations using ε_{WSe_2} obtained by fitting a single lorentzian to the A-exciton (a). Right column: calculations with the ε_{WSe_2} for the bulk material (b). R for the bare WSe_2 is shown in (c) and (g). R for WSe_2 on top of the spacer is shown in (d) and (h), a cavity mode appears around 500 nm, which can interact with the B-exciton. Then WSe_2 on top of the cavity without IBTs is shown in (e) and (i). The 3-component system is shown in (f) and (j).*

Hence, reflectivity was calculated for a layer of WSe_2 instead of molecules on top of the cavity. For that, both the complex dielectric function of bulk WSe_2 and a single Lorentzian fit to the A-exciton of the dielectric function were used. The fit was done to avoid contributions of the B-exciton (dip around 568 nm) and the rest of the background. It considered $\varepsilon_\infty = 17.5$, $\hbar\omega_{WSe_2} = 1.61$ eV, $f = 1$ and $\hbar\gamma_{WSe_2} = 0.17$ eV. The real and imaginary parts of the WSe_2 dielectric function and the single lorentzian fit to the A-exciton are shown in figure 5.10(a) and (b). Note that the $x-$axis is different for each one.

As before, the study of the reflectivity for each added layer is presented in figure 5.10. In (d) we can see an optical mode (dip around $\sim$ 500 nm) created by the spacer and the top layer. Such mode interacts with the B-exciton and the background in (h), absorbing more light.

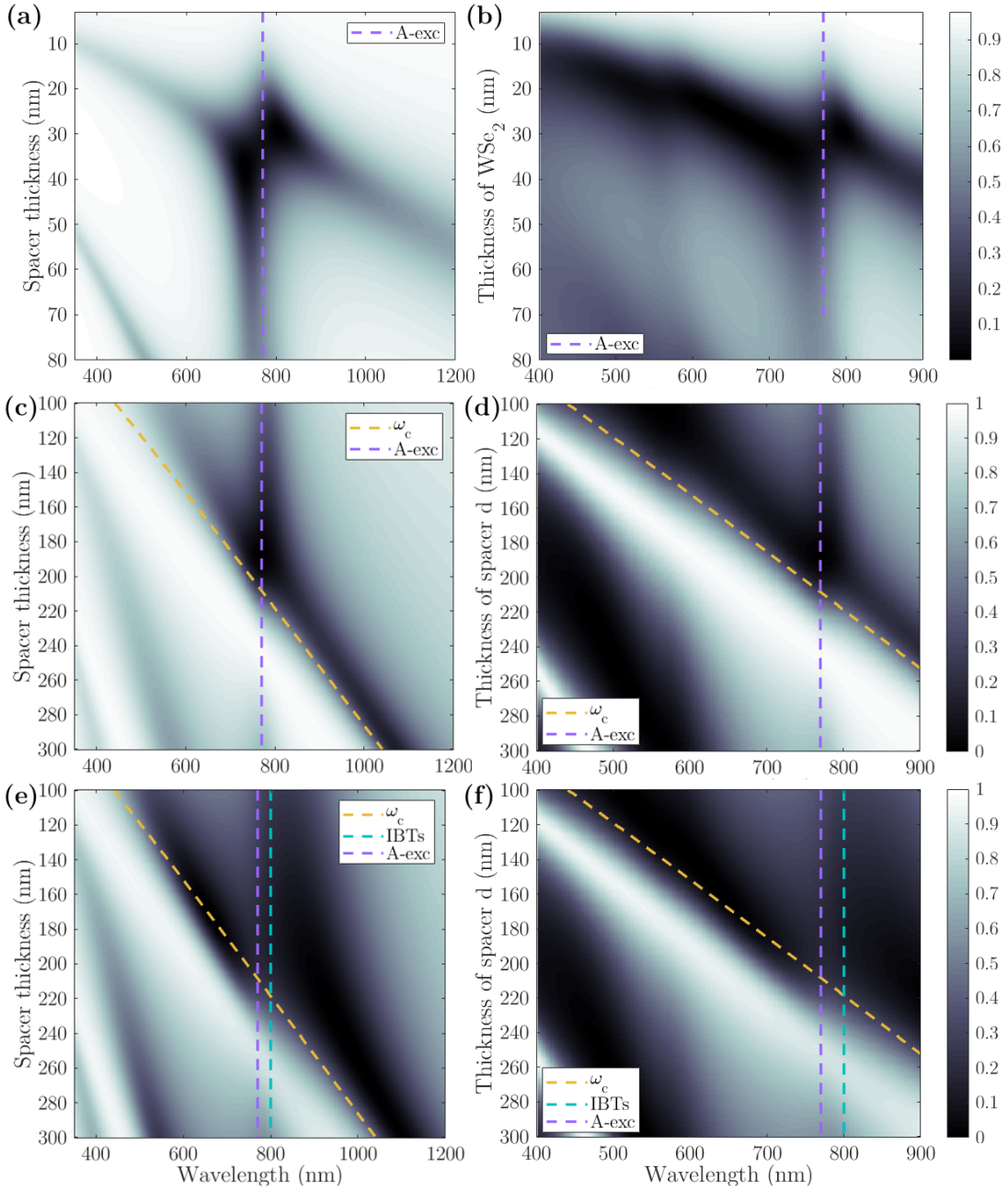

Figure 5.11: *Left column: Reflectivity calculations using ε of A-exciton Lorentz fit. Right column: calculations using ε_{WSe_2}. (a-b) WSe_2 thickness variation on top of the bottom mirror. (c-d) Variation in spacer thickness, for $h = 8$ nm, considering only Drude for Al. (e-f) Spacer thickness variation for $h = 8$ nm, considering also IBTs contribution.*

In the depicted case, the A-exciton is not in resonance with the optical mode (at $d = 200$ nm). The interaction causes dip broadening, as shown in (e). When taking into account also the IBTs the two peaks are clearly visible (f).

It is important to notice that the real part of the refractive index of WSe_2 is around $n \sim 4$ (fig. 5.10(b)), therefore it can hold cavity modes for thick enough

layers. WSe_2 is a layered material, the thickness of a monolayer is ~ 0.7 nm [34]. When WSe_2 is thick enough it couples to its own cavity mode, as shown in figure 5.11(a-b). In (b) the cavity mode interacts with the B-exciton for a thinner layer and with the A-exciton for a thicker one. For the calculations showed here $h = 8$ nm, such that around 10 layers in the material were considered. So that the cavity mode of the WSe_2 is far from the A-exciton (fig. 5.11(a-b)).

In this case, the cavity mode formed by WSe_2 is not used for any purpose, but it appears in the anticrossing spectra and it is an extra dip to be taken into account. For thicker layers of WSe_2 that mode starts interacting with the Al cavity mode, and the dip is red-shifted. Thicker layers (> 15 nm) are not considered here because the reflectivity spectra is complicated when both cavity modes, excitons and IBTs interact.

To strictly model the cavities with the layer of molecules or WSe_2 on top, and calculate its Rabi splitting, it is necessary to use a 3×3 Hamiltonian [32]. This is future work and it is not included in this manuscript.

The main idea of this section was to show that the open asymmetric cavity studied in this work could be used in a real system to strongly couple WSe_2 to light. Additionally, the IBTs seem to enhance the mode splitting. The experiment will be realized in the future and is not included in this work.

5.3 Potential of Light-IBT strongly coupled systems

As mentioned previously, plasmonic resonators allow to strongly couple light to other systems (as molecules or excitons of TMDs, to name a few) by using them as an *open cavity* [5]. Thus, light-IBT interactions in plasmonic resonators open an opportunity to couple three systems in a structure simple to fabricate, which could be useful to increase the coupling strength of the full system.

This comes to mind considering that, a strongly coupled system composed of nanoparticles (LSPR), an emitter (WS_2), and a microcavity resonance has shown to have larger coupling strength than any pair of them [32].

A similar idea was considered by the end of this work to enhance IBT-light interaction by adding another resonator on top. The calculations on the system show larger Rabi splitting for the 3-component system. Therefore, it will be considered for an experimental realization.

In this work only optical properties of the interacting system were measured, but those are not the only properties that may change under strong coupling.

The easiest experiment to test if Al is somehow different would be to measure its work function by Kelvin Probe Method. Because it is a characteristic that has already been shown to change in strongly coupled molecules [8]. The idea is to measure the top mirror work function for different thicknesses of the spacer.

Strongly coupled systems through cavities are coherent throughout the cavity, therefore there is non-locality involved. It is promising because Al has already interesting properties, such as being a superconductor. An open question is if it is possible to change the critical temperature of Al by strongly coupling it to a cavity.

Achieving strong IBT-light interactions in simple structures such as the ones considered here would be very interesting, due to the different properties that could be changed. The ultimate goal of strong IBT-light interactions in Al, is to tailor Al properties (as conductivity, critical temperature, work function, etc) just by fabricating it in a particular structure such as a nanodisk or forming an asymmetric cavity.

6

Conclusion and Outlook

This work focused on coupling light to spectrally localized interband transitions (IBTs) of Al through two different optical cavities: Al nanodisks as plasmonic nanoresonators, and Al asymmetric microcavities working as perfect absorbers.

Due to the fact that IBTs are an intrinsic transition of the material that composes the cavities, two resonances of different nature interact within the cavity. Thus it is in some sense a cavity coupled to itself. This makes it a system different from the ones usually studied by the strong-coupling community.

Given that it is a self-coupled system, modelling the dielectric constant of Al with Drude-Lorentz model was important to compare the uncoupled cavity and the IBT-cavity interaction.

Calculations were performed to model the coupling on both types of cavities. On the one hand, extinction and scattering spectra of single nanodisks was modelled in the quasi-static and modified long wavelength (MLWA) approximations. On the other hand, Transfer Matrix Method (TMM) at normal incidence was used for the calculations of the reflectivity spectra of the asymmetric microcavities.

The anticrossing in energy was observed for LSPR-IBT extinction spectra calculations. Nevertheless, due to the low quality of the deposited Al, the experimental data of nanodisks fabricated by HCL showed only weak interaction. The coupling strength was calculated by using the Coupled Oscillator Model (COM), and the experiments showed a $\sim 33\%$ weaker g than expected in calculations. By depositing Al at higher rates and lower vacuum we would be able to improve the experimental coupling strength to be on the edge of strong coupling. Only weak coupling can be claimed in the current system, which is enough to change the absorption rate of IBTs by only structuring Al in nanodisks.

Even though, single particle measurements were not reliable to discuss the IBT-LSPR coupling in those systems, the techniques for optical characterization of single particles are described in the text, since they were heavily used in this work.

In the case of asymmetric cavities, the interaction with the IBTs was observed in calculations and in experiments. Nonetheless, the interaction was weaker than in nanodisks, probably because the mode volume is more extended in the microcavities. However, in order to claim strong coupling, it is important to show mode splitting in absorption spectra, which was not clear for either structure. Therefore, both kinds of cavities are only weakly coupled, which enhances absorption by IBTs due to Purcell effect, but do not change material properties.

A surprising result from this work is that the asymmetric microcavity seems to be a promising platform for achieving strong coupling in open and extended cavities. This platform has the advantage that the emitter is not required to be placed in

between of the mirrors and that it is relatively easy to fabricate. Although IBTs increase the mode splitting, the emitter seems to strongly-couple to the cavity even without the need of IBTs. In that sense, this platform has a lot of potential.

Immediate future work involves the experimental realization of the system proposed in section 5.2.3. Which consists in coupling the A-exciton of WSe_2 to the asymmetric microcavity. These experiments are possible because during this thesis work I had the opportunity to learn to exfoliate and transfer 2D-TMDs. The experiments will be done to test if the asymmetric cavity is as good as the TMM calculations showed. The cavities with a few layers of WSe_2 on top will be measured in dispersion as discussed in section 4.3.

In the case of calculations it is necessary to finish the TMM code for oblique incidence. This will allow to make a direct comparison with the dispersion measurements mentioned above. It is also necessary to calculate the coupling strength of the system by using the 3×3 Coupled Oscillator Hamiltonian.

Measurements that would involve longer time and effort, but that would also be very interesting are conductivity, and work function of strongly-coupled Al. As well as superconducting properties of strongly-coupled Al, such as the critical temperature.

Another interesting follow up work involves different materials with spectrally localized IBTs, besides Al. Short experiments in Nickel and Niobium microcavities were also performed in this study. Nevertheless, the results are not included in this manuscript because they were not easy to understand in the short amount of time of the thesis. Also, improving the experimental techniques would require much more work, mainly because Nickel IBTs are in the UV region [10] and because Nb optical properties have not been widely studied [1]. The interest on Nb is also given by its superconducting characteristics.

In conclusion, the LSPR of Al nanodisks and microcavities as perfect absorbers are simple systems in which weak coupling to IBTs was achieved. This is enough to enhance light absorption by IBTs. Calculations show that by increasing Al quality it is possible to be on the edge of strong coupling in nanodisks. Nonetheless, in the case of microcavities, it may still not be enough to improve the coupling to the extended mode volume. It may be necessary to couple a third component, as molecules, to achieve strong-coupling. Surprisingly, asymmetric microcavities seem to be a promising platform to achieve strong-coupling in open cavities, even without the IBTs playing a role in the coupling.

Bibliography

[1] T. Wieduwilt, A. Tuniz, S. Linzen, S. Goerke, J. Dellith, U. Hübner, and M. A. Schmidt, "Ultrathin niobium nanofilms on fiber optical tapers – a new route towards low-loss hybrid plasmonic modes," *Scientific Reports*, vol. 5, p. 17060, dec 2015.

[2] A. D. Rakić, "Algorithm for the determination of intrinsic optical constants of metal films: application to aluminum," *Applied Optics*, vol. 34, p. 4755, aug 1995.

[3] A. Fox and A. Fox, "Optical Properties of Solids (Oxford Master Series in Condensed Matter Physics)," 2001.

[4] D. G. Baranov, M. Wersäll, J. Cuadra, T. J. Antosiewicz, and T. Shegai, "Novel Nanostructures and Materials for Strong Light-Matter Interactions," 2018.

[5] P. Törmä and W. L. Barnes, "Strong coupling between surface plasmon polaritons and emitters: a review," *Reports on Progress in Physics*, vol. 78, p. 013901, jan 2015.

[6] D. S. Dovzhenko, S. V. Ryabchuk, Y. P. Rakovich, and I. R. Nabiev, "Light–matter interaction in the strong coupling regime: configurations, conditions, and applications," *Nanoscale*, vol. 10, pp. 3589–3605, feb 2018.

[7] B. Munkhbat, M. Wersäll, D. G. Baranov, T. J. Antosiewicz, and T. Shegai, "Suppression of photo-oxidation of organic chromophores by strong coupling to plasmonic nanoantennas," *Science Advances*, vol. 4, p. eaas9552, jul 2018.

[8] J. A. Hutchison, A. Liscio, T. Schwartz, A. Canaguier-Durand, C. Genet, V. Palermo, P. Samorì, and T. W. Ebbesen, "Tuning the Work-Function Via Strong Coupling," *Advanced Materials*, vol. 25, pp. 2481–2485, may 2013.

[9] O. Lecarme, Q. Sun, K. Ueno, and H. Misawa, "Robust and Versatile Light Absorption at Near-Infrared Wavelengths by Plasmonic Aluminum Nanorods," *ACS Photonics*, vol. 1, pp. 538–546, jun 2014.

[10] Z. Pirzadeh, T. Pakizeh, V. Miljkovic, C. Langhammer, and A. Dmitriev, "Plasmon–Interband Coupling in Nickel Nanoantennas," *ACS Photonics*, vol. 1, pp. 158–162, mar 2014.

[11] M. W. Knight, N. S. King, L. Liu, H. O. Everitt, P. Nordlander, and N. J. Halas, "Aluminum for Plasmonics," *ACS Nano*, vol. 8, pp. 834–840, jan 2014.

[12] A. Mario and A. Alu, *Optical Antennas*. Cambridge University Press, 2013.

[13] I. R. Hooper and W. L. Barnes, "The Basics of Plasmonics," *Handbook of Surface Science*, vol. 4, pp. 37–74, jan 2014.

[14] C. F. Bohren and D. R. Huffman, *Absorption and scattering of light by small particles*. Wiley, 2004.

[15] M. Meier and A. Wokaun, "Enhanced fields on large metal particles: dynamic depolarization," *Optics Letters*, vol. 8, p. 581, nov 1983.

[16] I. Zoric, M. Zach, B. Kasemo, and C. Langhammer, "Gold, Platinum, and Aluminum Nanodisk Plasmons: Material Independence, Subradiance, and Damping Mechanisms," *ACS Nano*, vol. 5, pp. 2535–2546, apr 2011.

[17] M. Born and E. Wolf, *Principles of optics : electromagnetic theory of propagation, interference and diffraction of light*. Cambridge University Press, 1999.

[18] Z. Li, E. Palacios, S. Butun, H. Kocer, and K. Aydin, "Omnidirectional, broadband light absorption using large-area, ultrathin lossy metallic film coatings," *Scientific Reports*, vol. 5, p. 15137, dec 2015.

[19] C. C. C. C. Gerry and P. P. L. Knight, *Introductory quantum optics*. Cambridge University Press, 2005.

[20] F. Marquier, C. Sauvan, and J.-J. Greffet, "Revisiting Quantum Optics with Surface Plasmons and Plasmonic Resonators," *ACS Photonics*, vol. 4, pp. 2091–2101, sep 2017.

[21] J. Galego, F. J. Garcia-Vidal, and J. Feist, "Cavity-Induced Modifications of Molecular Structure in the Strong-Coupling Regime," *Physical Review X*, vol. 5, p. 041022, nov 2015.

[22] M. Wersäll, J. Cuadra, T. J. Antosiewicz, S. Balci, and T. Shegai, "Observation of Mode Splitting in Photoluminescence of Individual Plasmonic Nanoparticles Strongly Coupled to Molecular Excitons," *Nano Letters*, vol. 17, pp. 551–558, jan 2017.

[23] A. J. Moilanen, T. K. Hakala, and P. Törmä, "Active Control of Surface Plasmon-Emitter Strong Coupling," *ACS Photonics*, vol. 5, no. 1, pp. 54–64, 2018.

[24] L. Novotny, "Strong coupling, energy splitting, and level crossings: A classical perspective," *American Journal of Physics*, vol. 78, no. 11, pp. 1199–1202, 2010.

[25] T. Pakizeh, C. Langhammer, I. Zoric, P. Apell, and M. Kall, "Intrinsic Fano Interference of Localized Plasmons in Pd Nanoparticles," *Nano Letters*, vol. 9, pp. 882–886, feb 2009.

[26] T. Pakizeh, "Optical Absorption of Plasmonic Nanoparticles in Presence of a Local Interband Transition," *The Journal of Physical Chemistry C*, vol. 115, pp. 21826–21831, nov 2011.

[27] M. Schwind, B. Kasemo, and I. Zoric, "Localized and Propagating Plasmons in Metal Films with Nanoholes," *Nano Letters*, vol. 13, pp. 1743–1750, apr 2013.

[28] H. Fredriksson, Y. Alaverdyan, A. Dmitriev, C. Langhammer, D. S. Sutherland, M. Zäch, and B. Kasemo, "Hole-mask colloidal lithography," *Advanced Materials*, vol. 19, no. 23, pp. 4297–4302, 2007.

[29] G. Zengin, M. Wersäll, S. Nilsson, T. J. Antosiewicz, M. Käll, and T. Shegai, "Realizing Strong Light-Matter Interactions between Single-Nanoparticle Plasmons and Molecular Excitons at Ambient Conditions," *Physical Review Letters*, vol. 114, p. 157401, apr 2015.

[30] P. T. Kristensen and S. Hughes, "Modes and Mode Volumes of Leaky Optical Cavities and Plasmonic Nanoresonators," *ACS Photonics*, vol. 1, pp. 2–10, jan 2014.

[31] M.-N. Su, P. D. Dongare, D. Chakraborty, Y. Zhang, C. Yi, F. Wen, W.-S. Chang, P. Nordlander, J. E. Sader, N. J. Halas, and S. Link, "Optomechanics of Single Aluminum Nanodisks," *Nano Letters*, vol. 17, pp. 2575–2583, apr 2017.

[32] A. Bisht, J. Cuadra, M. Wersäll, A. Canales, T. J. Antosiewicz, and T. Shegai, "Universal method for realization of strong light-matter coupling in hierarchical microcavity-plasmon-exciton systems," jun 2018.

[33] T. J. Antosiewicz, S. P. Apell, and T. Shegai, "Plasmon–Exciton Interactions in a Core–Shell Geometry: From Enhanced Absorption to Strong Coupling," *ACS Photonics*, vol. 1, pp. 454–463, may 2014.

[34] A. Arora, M. Koperski, K. Nogajewski, J. Marcus, C. Faugeras, and M. Potemski, "Excitonic resonances in thin films of WSe2: from monolayer to bulk material," *Nanoscale*, vol. 7, pp. 10421–10429, jun 2015.